DOE/SERI-9234/3
(DE81030370)

PHOTOVOLTAIC MECHANISMS IN POLYCRYSTALLINE THIN FILM SILICON SOLAR CELLS

Quarterly Technical Progress Report No. 3 for February 1—April 30, 1981

By
Bhushan Sopori

Work Performed Under Contract No. AC02-77CH00178

Motorola, Inc.
Phoenix, Arizona

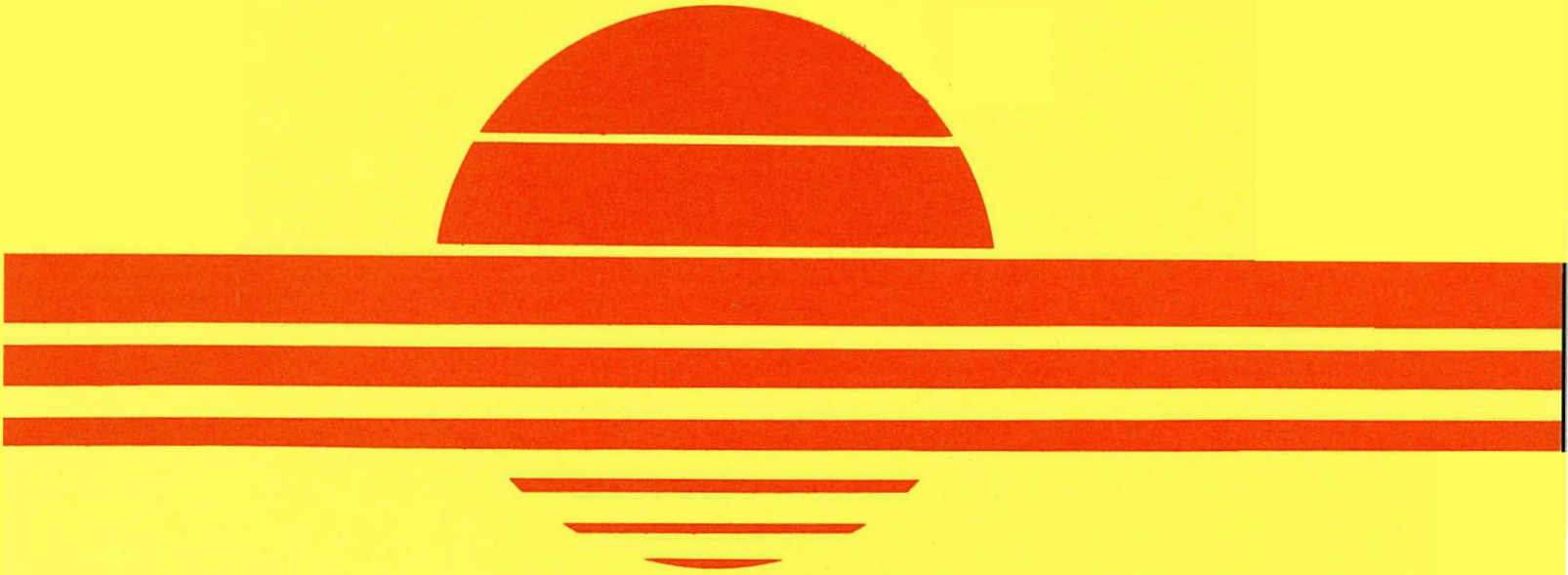

U.S. Department of Energy

Solar Energy

DISCLAIMER

Available from the National Technical Information Service, U. S. Department of Commerce, Springfield, Virginia 22161.

Price: Printed Copy A03
Microfiche A01

Codes are used for pricing all publications. The code is determined by the number of pages in the publication. Information pertaining to the pricing codes can be found in the current issues of the following publications, which are generally available in most libraries: *Energy Research Abstracts, (ERA); Government Reports Announcements* and Index (*GRA* and I); *Scientific and Technical Abstract Reports (STAR);* and publication, NTIS-PR-360 available from (NTIS) at the above address.

DOE/SERI-9234/3
(DE81030370)
Distribution Category UC-63

PHOTOVOLTAIC MECHANISMS IN POLYCRYSTALLINE THIN FILM SILICON SOLAR CELLS

QUARTERLY TECHNICAL PROGRESS REPORT NO. 3

FOR PERIOD

1 FEBRUARY 1981 - 30 APRIL 1981

BHUSHAN SOPORI

SUB-CONTRACT NO. XZ-0-9234

START DATE 7/30/80
COMPLETION DATE 8/29/81

PREPARED BY

MOTOROLA, INC.
SOLAR ENERGY DEPARTMENT
5005 EAST McDOWELL ROAD
PHOENIX, ARIZONA 85008

PREPARED FOR

UNITED STATES
DEPARTMENT OF ENERGY
DIVISION OF SOLAR TECHNOLOGY
AND
SOLAR ENERGY RESEARCH INSTITUTE

MOTOROLA PROJECT NO. 2386

TABLE OF CONTENTS

LIST OF FIGURES

1.0 INTRODUCTION

In previous reports it has been shown that the intragrain structure in large grain polycrystalline silicon substrates can play a domainant role in limiting the performance of solar cells fabricated on such substrates. It was also shown that, in RTR ribbons, dislocations are responsible for the major intragrain defects. Earlier analyses, using defect etching on a bevelled sample and depth profiling of dislocation paths by step etching, has led to the categorization of dislocations in RTR ribbons into two groups: (i) isolated line dislocations and (ii) dislocation networks. During this contract period our major effort was devoted towards developing a technique for rapid identification of these two types of dislocations -- to be followed in the future by isolating their effects on cell performance. This has been accomplished by extending the technique of Cu decoration to determine defect propagation in polycrystalline substrates.

Another area of emphasis was a study of the influence of surface preparation on cell performance. Two approaches were pursued in this direction. (1) cells were fabricated on differently prepared substrates consisting of sequential wafers from a Wacker Silso ingot. These included (a) damage-free polished (b) chem etched and (c) textured. (2) An analysis of the effects of texturing on cell performance has been started. The objective of this analysis is to establish theoretical approaches for the optimum design of a textured cell. Various aspects of texturing have been studied, starting with the analysis and design of the simpler case of single crystal cells.

This report describes two areas of research carried out during this contract period. Results of Cu decoration for defect analysis are given in Section 2. Section 3 discusses the design of an AR coating for optimizing performance of a textured cell. Basic optical characteristics of textured surfaces utilized in this design are described in the appendix.

2.0 COPPER DECORATION FOR OBSERVATION OF DISLOCATIONS

Decoration of dislocations by copper was used by Dash to observe dislocation paths in Czochralski single crystal silicon (1). Although this technique appears to be quite unique, it has only been used under very restricted conditions of low dislocation density ($\sim 10^{3} cm^{-2}$) and specific orientation which will permit viewing along a <111> direction. Very little information is available to render this technique suitable for more general cases. We have pursued this technique to study dislocations in RTR ribbons. This section presents some preliminary results of our investigations.

2.1 PROCEDURE

Samples, typically 2 cm x 1 cm were scribed out of RTR ribbons (~8 mils thick). Two different approaches were used to diffuse Cu into the samples. In one case samples were etched for 15 minutes in Wright etch and a thin film of Cu was deposited on one side. In the other case Cu was deposited directly on one of the ribbon surfaces. Cu was diffused into the sample at 900°C in a hydorgen atmosphere. Alternatively, a layer of SiO_2 was sputtered on the copper side of the sample and diffusion carried out at 900°C in a forming gas ambient. Following Cu diffusion, the residual SiO_2 and/or Cu was etched off and the samples examined under VIS/IR microscopes. Some Cu diffused samples were laser scribed into strips (8 mm long) and the two surfaces normal to the surface of Cu deposition (i.e. through the thickness of the ribbon) were polished for viewing under an IR microscope.

2.2 RESULTS

Figure 2.1 shows a photograph of a Cu diffused sample, which was defect etched on one side prior to Cu deposition and observed under an IR microscope with the etched side towards the objective lens. The presence of Cu precipitation on dislocations is seen as long "tails" associated with many of the etch pits. Many

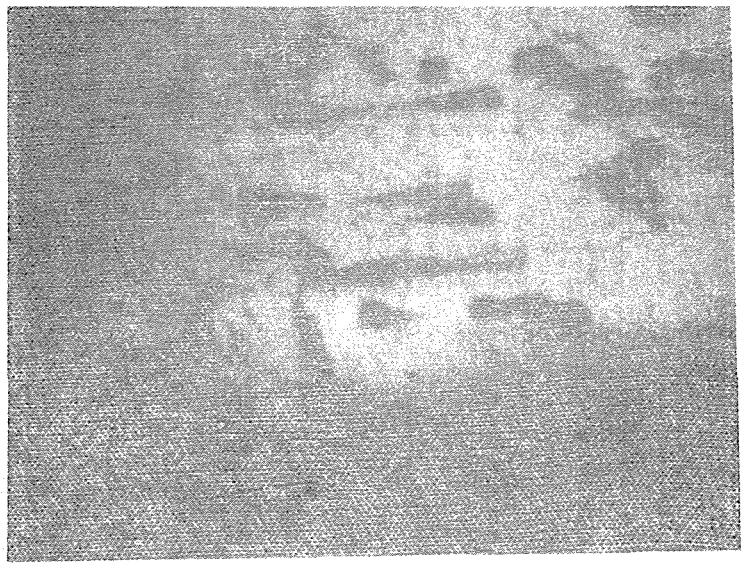

Shadowing due to grain boundary

FIGURE 2.1: IR microscopic picture of Cu decoration at dislocations.

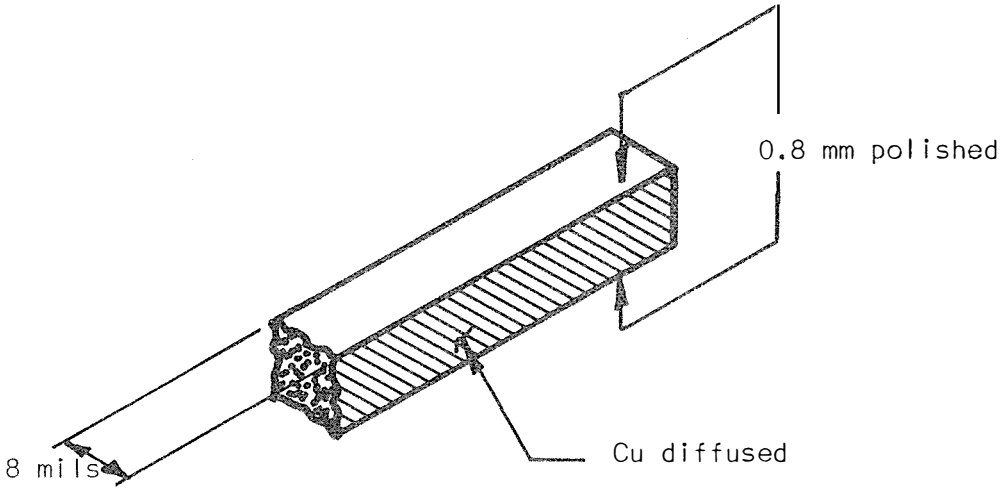

FIGURE 2.2a: CONFIGURATION FOR VIEWING DISLOCATIONS IN THE BULK.

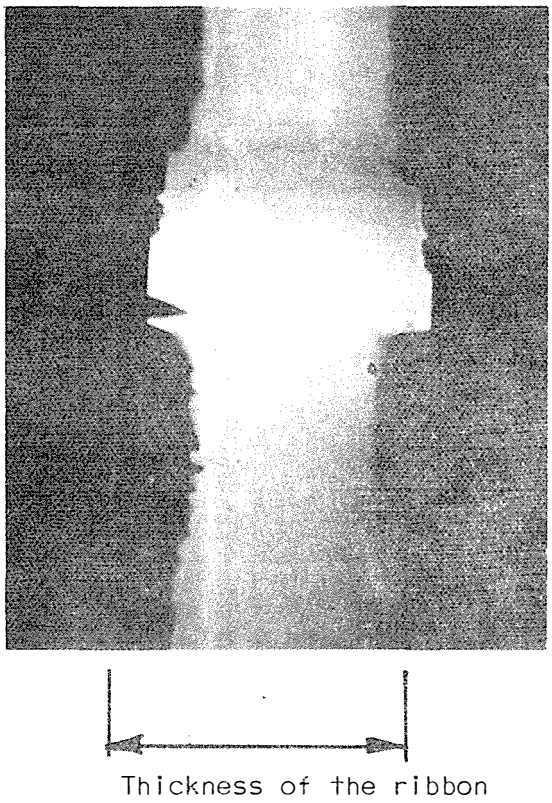

FIGURE 2.2b: IR PHOTOGRAPH TAKEN IN A TRANSMISSION MODE SHOWING LACK OF Cu PRECIPITATION IN THE BULK OF THE SAMPLE.

dislocation networks and loops can be seen in this figure. It should be pointed out that due to the high magnification used for viewing copper precipitation, the depth of forcus is quite small (which leads to the formation of the tails seen in figure 2.1.* Hence observation of Cu precipitation, in this configuation is rather limited to a region near the surface.

Attempts were also made to observe dislocation lines throughout the thickness of the ribbon. Figure 2.2a shows the sample viewing configuration used for this purpose and figure 2.2b shows a photograph of the sample taken in the transmission mode. As seen in this figure there is no evidence of Cu precipitation in the bulk of the sample, although some dislocation pits are clearly seen. Initial thickness of the sample (i.e. prior to defect etching) is also shown in figure 2.2b. The dark edges are due to a high density of etch pits as well as copper precipitation which extends a small distance away from the edges of the etch pits. Further investigations were needed to improve dislocation observations in this configuration.

Experiments carried out on an unetched sample gave very interesting (perhaps very useful) results. It was found that Cu alloyed at certain sites and could not be dissolved in aqua regia. Figure 2.3 is a series of photographs of a sample surface showing Cu-alloyed sites. The pattern of the sites indicates that the sites of Cu-alloy may be the dislocation sites. This hypothesis was confirmed by comparing this pattern with the etch pit pattern of an adjacent (un-diffused) sample. Figures 2.4a and 2.4b show photographs of two corresponding regions from Cu-diffused and defect etched samples respectively. Figure 2.4 clearly indicates that not all dislocation sites have Cu alloyed in. To investigate it further, a Cu-alloyed sample was Wright etched to reveal the dislocations. Figure 2.5 is a

---

*An oil immersion lens was used for taking the photograph of figure 2.1. This also interfered in taking photographs of etch pits in the reflection mode.

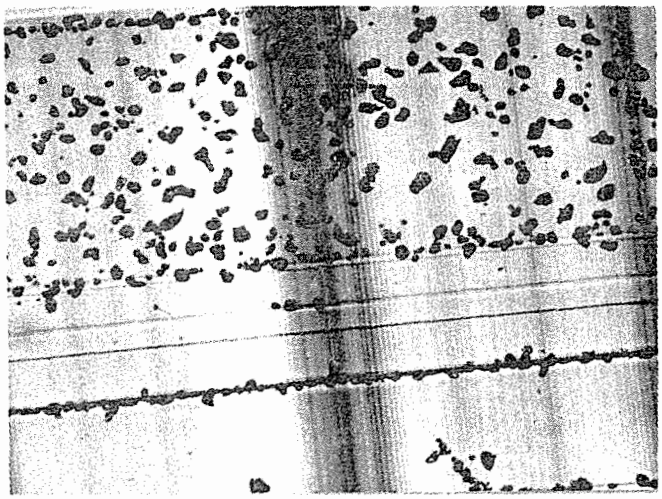

(a)

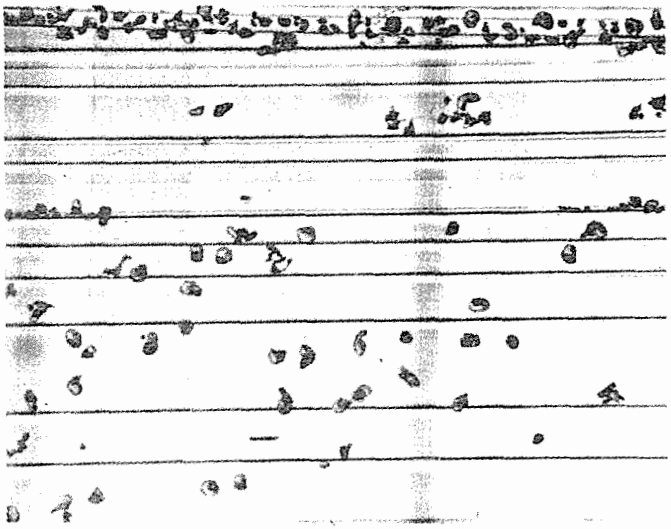

(b)

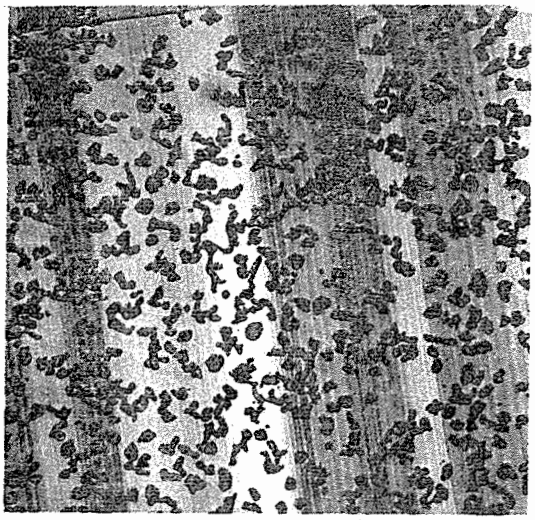

(c)

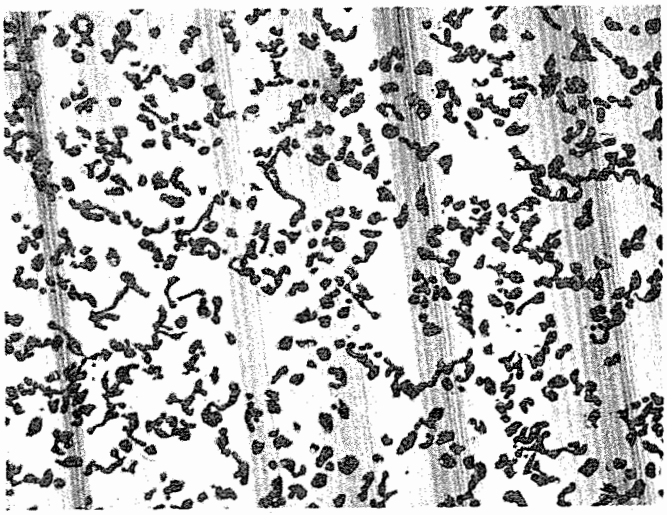

(d)

FIGURE 2.3: PHOTOGRAPHS OF SEVERAL REGIONS OF A Cu DIFFUSED SAMPLE SHOWING Cu-ALLOYED SITES.

photograph of a region of the sample which shows that etch pits are formed in the regions which do not show residual Cu-alloy (etch pits with light central core are the sites of Cu-alloy). Although several explanations can be forwarded to explain why only some dislocations show heavy Cu diffusion/alloying, further work needs to be carried out to confirm these views.

These results on Cu diffusion for the observation of dislocations in a more general manner indicate that this technique may allow categorization of dislocations into "active" and "not-so-active" groups.

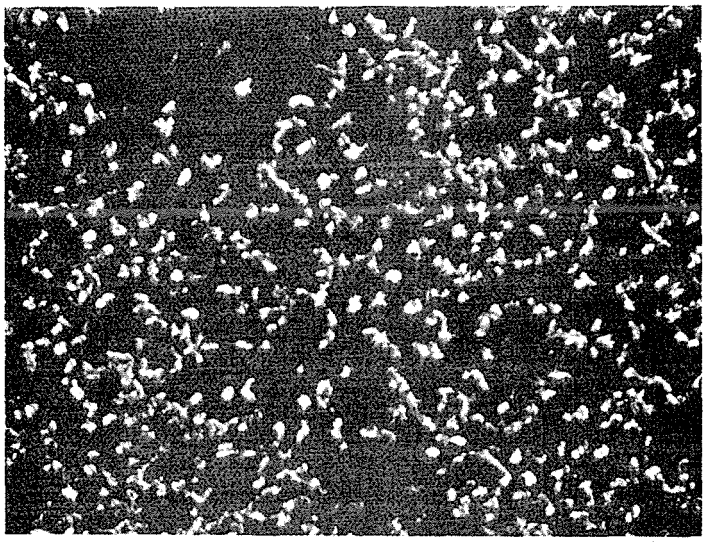

Cu-DIFFUSED

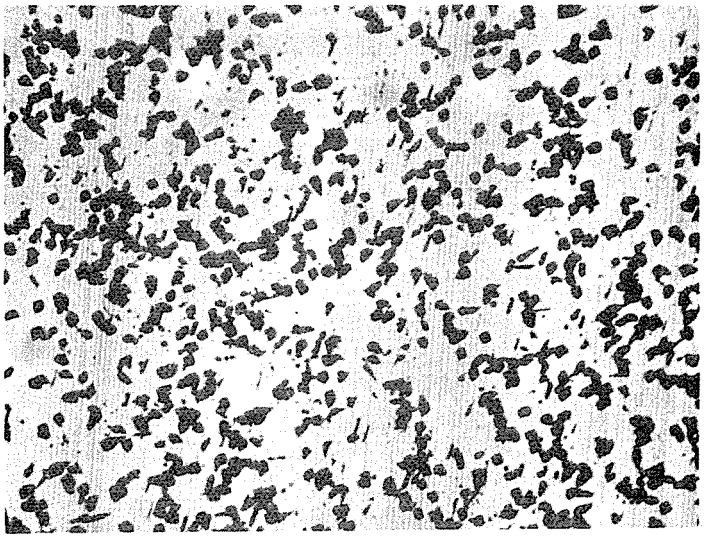

DEFECT-ETCHED

FIGURE 2.4a

FIGURE 2.4: PHOTOGRAPHS COMPARING THE PATTERNS DUE TO Cu-ALLOYED SITES WITH THE ETCH-PIT PATTERN IN THE ADJACENT REGIONS OF AN RTR RIBBON.

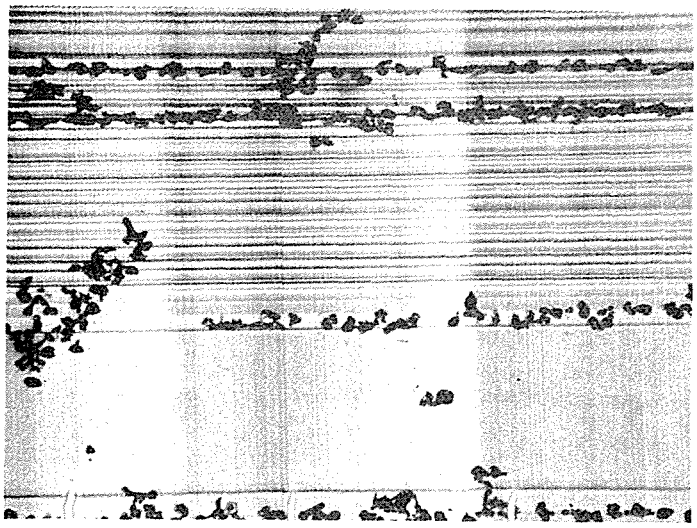

Cu-DIFFUSED

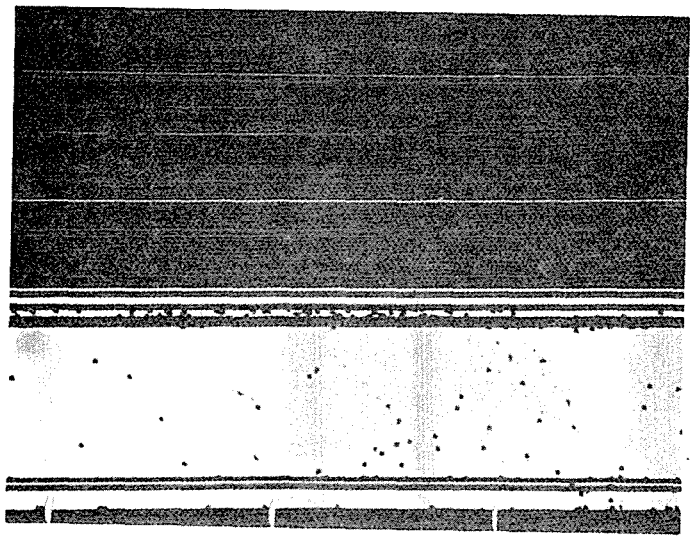

WRIGHT ETCHED

FIGURE 2.4b

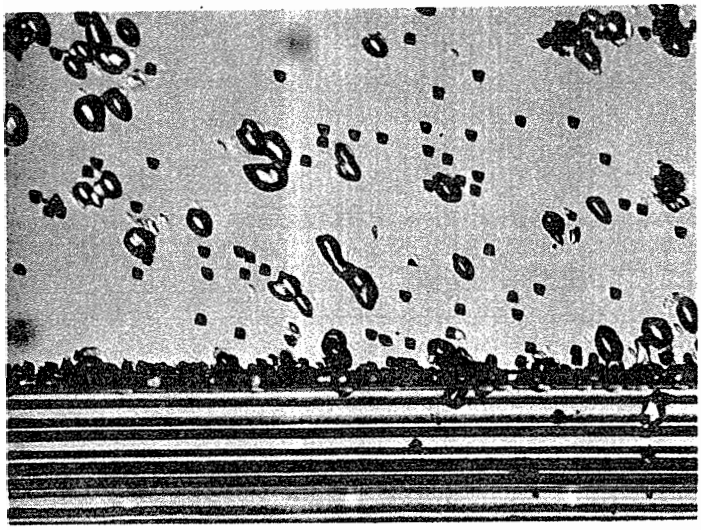

FIGURE 2.5: PHOTOGRAPH SHOWING ETCH PITS IN A Cu-DIFFUSED SAMPLE. ETCH PITS WITH LIGHT CORE ARE THE SITES OF Cu-ALLOY.

3.0 DESIGN OF AR COATINGS FOR TEXTURED SOLAR CELLS

Solar cells are large area optical devices which require efficient broad-band, optical coupling utilizing minimum cost. The multiple thin film coating approach, used conventionally for broad-band antireflection, is not compatible with low-cost cell fabrication processes. An alternate approach developed recently for silicon solar cells consists of texture etching <100> oriented silicon wafers prior to the cell fabrication (2,3). Texturing generates a pseudo-periodic surface structure (pyramids) which can lower the net surface reflection and also refract the incident light in a way that increases the effective absorption within the bulk of the cell. A well textured (100) oriented silicon surface can lower the average reflectance (weighted with respect to the incident useful solar spectrum) to about 0.1. Reflection can be further reduced to ~0.03 by depositing a matched thin film coating on the textured surface. A proper design of such a coating can, additionally, optimize the cell performance to a given input specturm. However, to-date no quantitative analysis has been done which can be used to design a thin film coating for a textured cell (of known characteristics). This section describes a procedure for the design of an AR coating matched to optimize the performance of a textured solar cell. The procedure is based on a known variation of the internal quantum efficiency of a textured cell as a function of the photon wavelength. The design consists of calculating the variation in the integrated external quantum efficiency, $\langle \eta_E \rangle$, as a function of the thickness of an AR film; the thickness that leads to maximum $\langle \eta_E \rangle$ is the desired thickness. The requirements for the choice of the suitable film(s) are discussed in terms of the optical parameters of the film(s) as well as the potential of low-cost technology for their deposition.

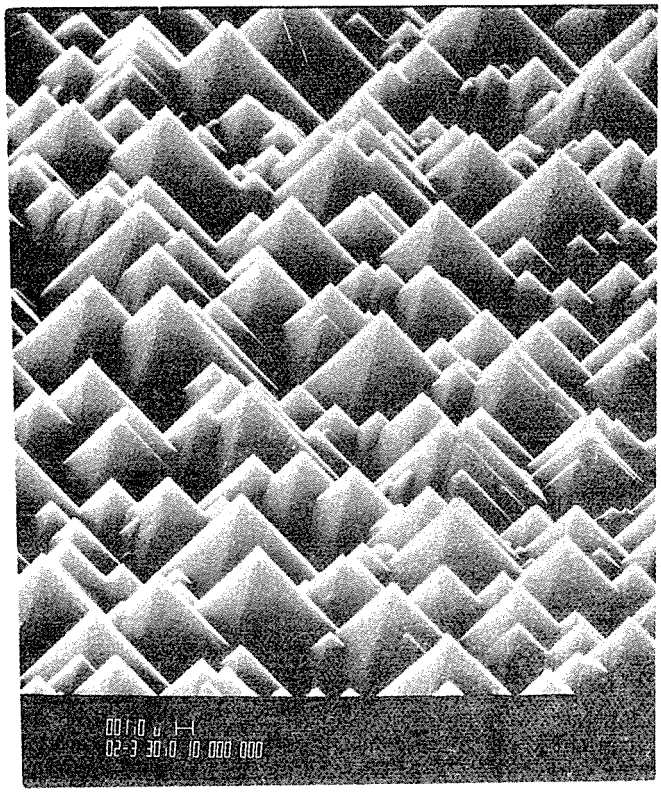

FIGURE 3.1: SEM PHOTOGRAPH OF A TEXTURED SURFACE

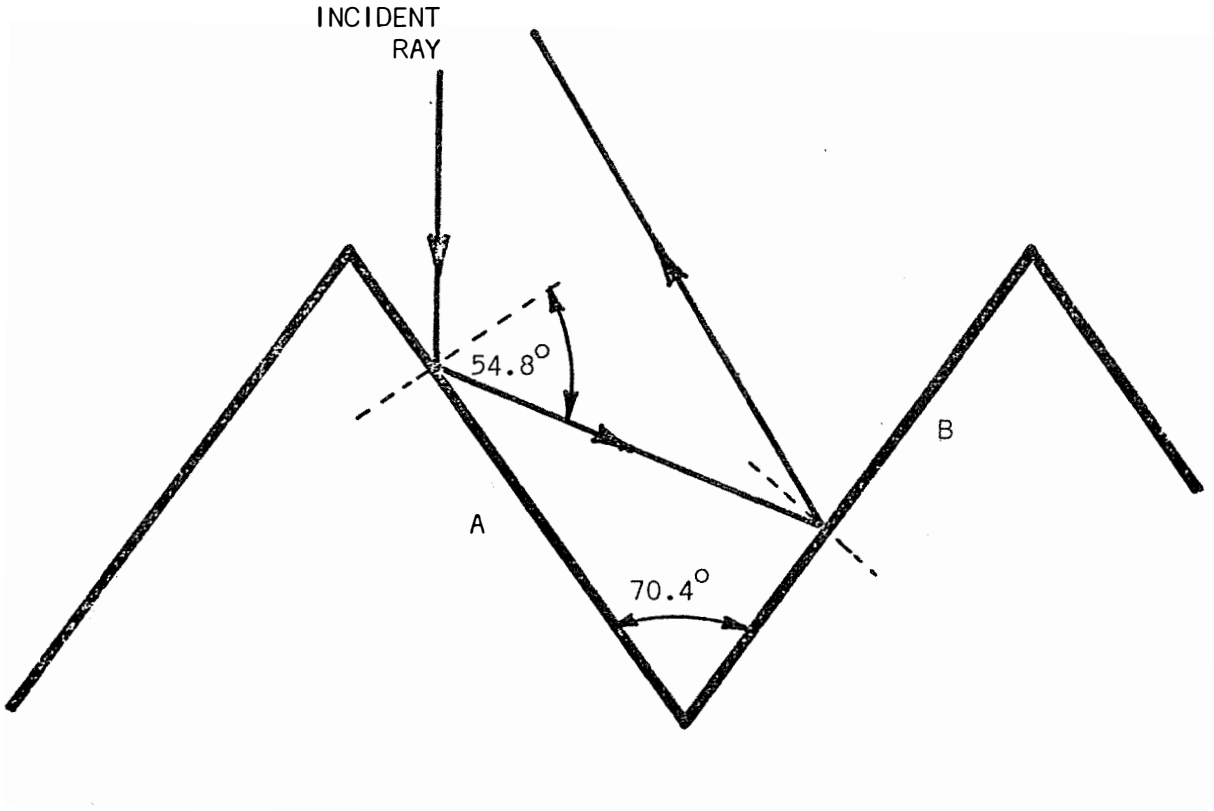

FIGURE 3.2: ILLUSTRATION SHOWING RAY PROPAGATION AT ONE GRATING COMPONENT.

This section first briefly describes the basic characteristics of (100) textured surfaces, followed by a ray optics approach towards the analysis of textured surfaces (uncoated and coated). The technique of optimization will be demonstrated for two practical cases of solar cells viz a standard cell and a u-v cell.

3.1 CHARACTERISTICS OF TEXTURED SURFACES

Texturing (100) silicon surfaces by etchants like hydrazine or alkali hyderoxide solutions, is known to generate regular arrays of pyramids, with an apex angle of 70.4°, by exposing (111) surfaces. Figure 3.1 shows an SEM photograph of a textured silicon surface with a pyramid height of $\simeq$15µm. The pyramid height, hence the spacing between them, can be controlled by controlling the etch composition. It has been shown earlier that due to the regularity of the surface structures, a textured surface may be regarded as a two-dimensional grating (psuedo periodic structure). A ray optics approach has been developed to determine the optical characteristics of textured surfaces. In this approach the two-dimensional grating is resolved into two orthogonal spatial components, x and y. Characteristics of each grating component are analysed using the ray optics approach and the total characteristics are determined by averaging the contributions due to the individual components. In this section we will present the basic equations for the ray optical analysis -- the procedure will be described only for the case where the light in normally incident to the surface.

Figure 3.2 shows a schematic representation of one of the grating components. The optical ray path for evaluating reflection characteristics is shown for the normal incidence. The incident light ray makes an angle of 54.8° with the pyramid wall A. Following the reflection from A, the light beam is re-reflected from wall B. The net reflection coefficient, R, is given by:

$$R = R_A \cdot R_B \tag{1}$$

where R_A and R_B are the reflection coefficients at the surfaces A and B respectively. Since the incident light is unpolarized, the above equation applies to parallel and perpendicular components, and the net reflection coefficient is given by

$$R = \frac{R_{\parallel} + R_{\perp}}{2} = \frac{R_{A\parallel} \cdot R_{B\parallel} + R_{A\perp} \cdot R_{B\perp}}{2} \tag{2}$$

Where the subscripts $\parallel$ and $\perp$ refer to the parallel and the perpendicular components respectively, $R_{m\parallel}$ and $R_{m\perp}$ (where m = A,B) are given by Fresnel equations

$$R_{m\parallel} = \frac{n_3 \cos\theta_{im} - n_0 \cos\theta_{tm}}{n_3 \cos\theta_{im} + n_0 \cos\theta_{tm}} \tag{3}$$

$$R_{m\perp} = \frac{n_0 \cos\theta_{im} - n_3 \cos\theta_{tm}}{n_0 \cos\theta_{im} + n_3 \cos\theta_{tm}} \tag{4}$$

where the subscripts i and t refer to incident and the transmitted beams respectively. In the above equation $\theta_{iA} = 54.8^{o}$, $\theta_{iB} = 16.7^{o}$ and n_0 and n_3 are the refractive indeces for air and silicon respectively. Notice that n_3 is in general complex and depends on the wavelength i.e. $n_3(\lambda) = n_3' - ik_3$. The wavelength dependence of n_3' and k_3 are published in the literature (4).

An analysis similar to this also applies to the second spatial grating component. For normal incidence the magnitude of the reflection coefficients for both components remain the same. We have calculated the total reflection coefficient as a function of wavelength using the published data on the wavelength dependence of the complex index. These results are shown in figure 3.3.

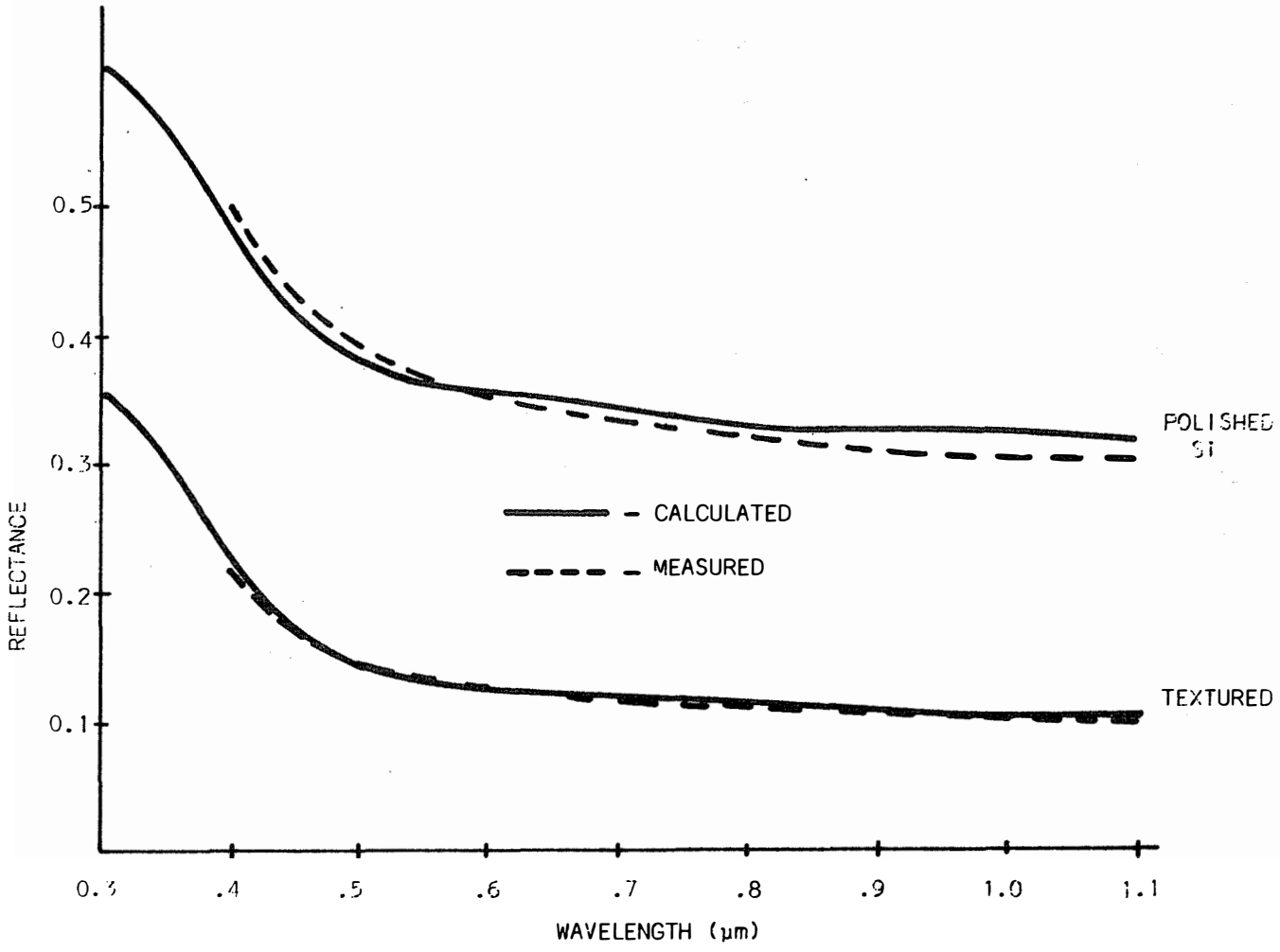

FIGURE 3.3: A COMPARISON OF THE CALCULATED DEPENDENCE OF THE REFLECTION COEFFICIENTS OF POLISHED AND TEXTURED SURFACE WITH THE MEASURED VALUES.

Figure 3.3 also shows the calculated variation of the reflection coefficient for polished silicon. To confirm the validity of the calculated results we have shown the measured reflection coefficient for polished and textured surfaces. These measurements were made with a Cary 17 spectrometer using integrating spheres. The back surface reflections were minimized by using a totally absorbing layer on the back side of the sample.

The ray optics approach can also be used to determine the refraction characteristics i.e. the beam propagation into the bulk of the cell. Ray propagation, based on the direct observation of the transmitted beam has been described elsewhere (see appendix). In the present context this angular dispersion is implicitly included in the given spectral response (i.e. internal quantum efficiency) of the cell for which the AR coating has been optimized.

Previous analysis can be extended to a single or multilayer thin film coating deposited on the textured surface. Of particular interest is a case where the coating consists of two layers. Although the treatment presented here for the two layer coating is general, the calculated results will be presented for a system of Si_3N_4/SiO_2/textured cell. Basis for the choice of this system will be discussed in the later section. The configuration for the calculation of the reflection coefficient is shown in figure 3.4.

Reflection coefficient at wall A, R_A, is given by

$$R_A = \frac{r_1 + A \exp\left[-\frac{i4\pi}{\lambda} n_1 t_1 \cos\theta_1\right]}{1 + r_1 A \exp\left[-i4\pi/\lambda \cdot n_1 t_1 \cos\theta_1\right.} \qquad (5)$$

where

$$A = \frac{r_2 + r_3 \exp\left[-i4\pi/\lambda\, n_2 t_2 \cos\theta_2\right]}{1 + r_2 r_3 \exp\left[-i4\pi/\lambda\, n_2 t_2 \cos\theta_2\right]} \qquad (6)$$

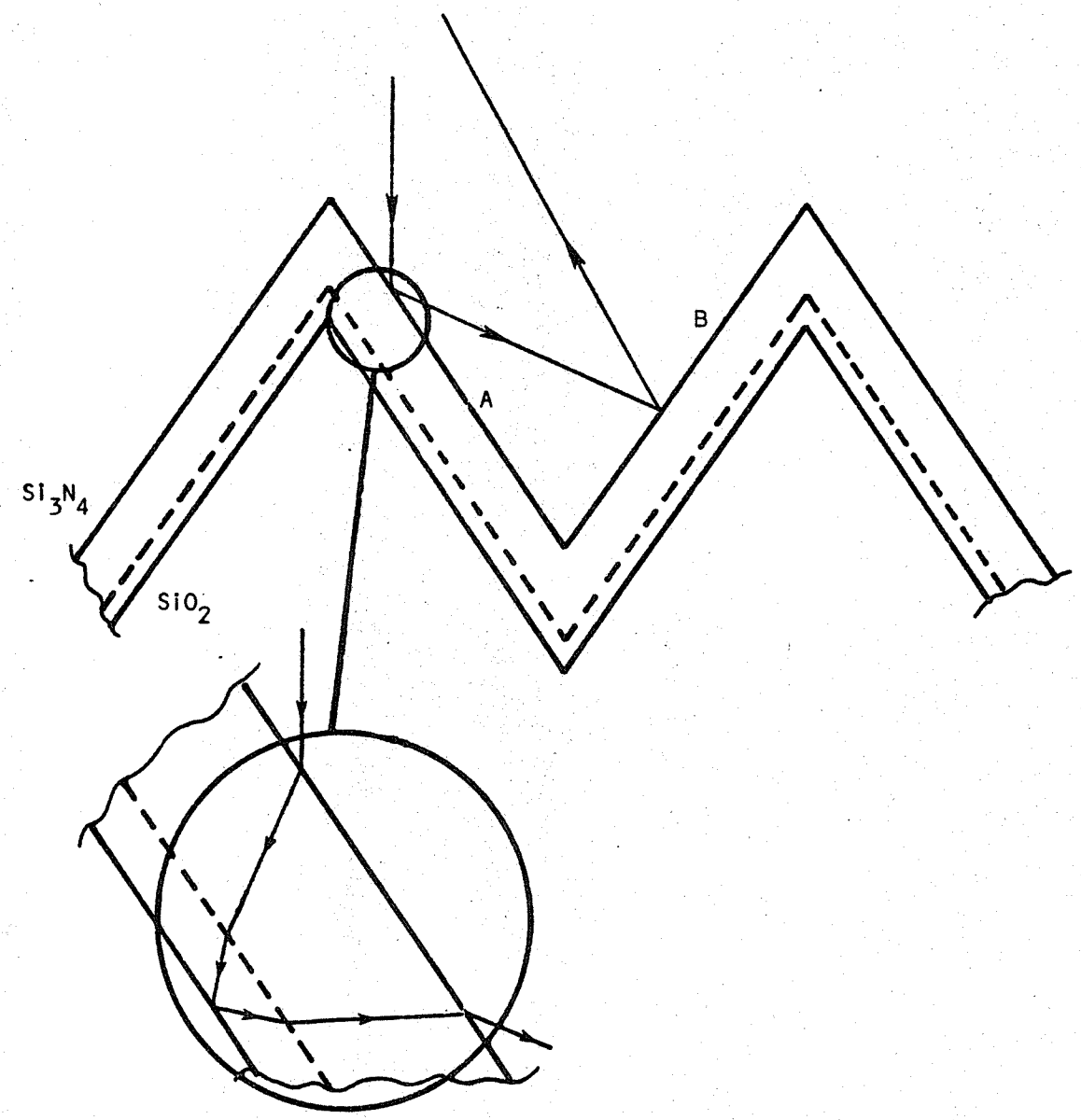

FIGURE 3.4: SCHEMATIC OF RAY PROPAGATION PATH AT AN AR COATED TEXTURED SURFACE.

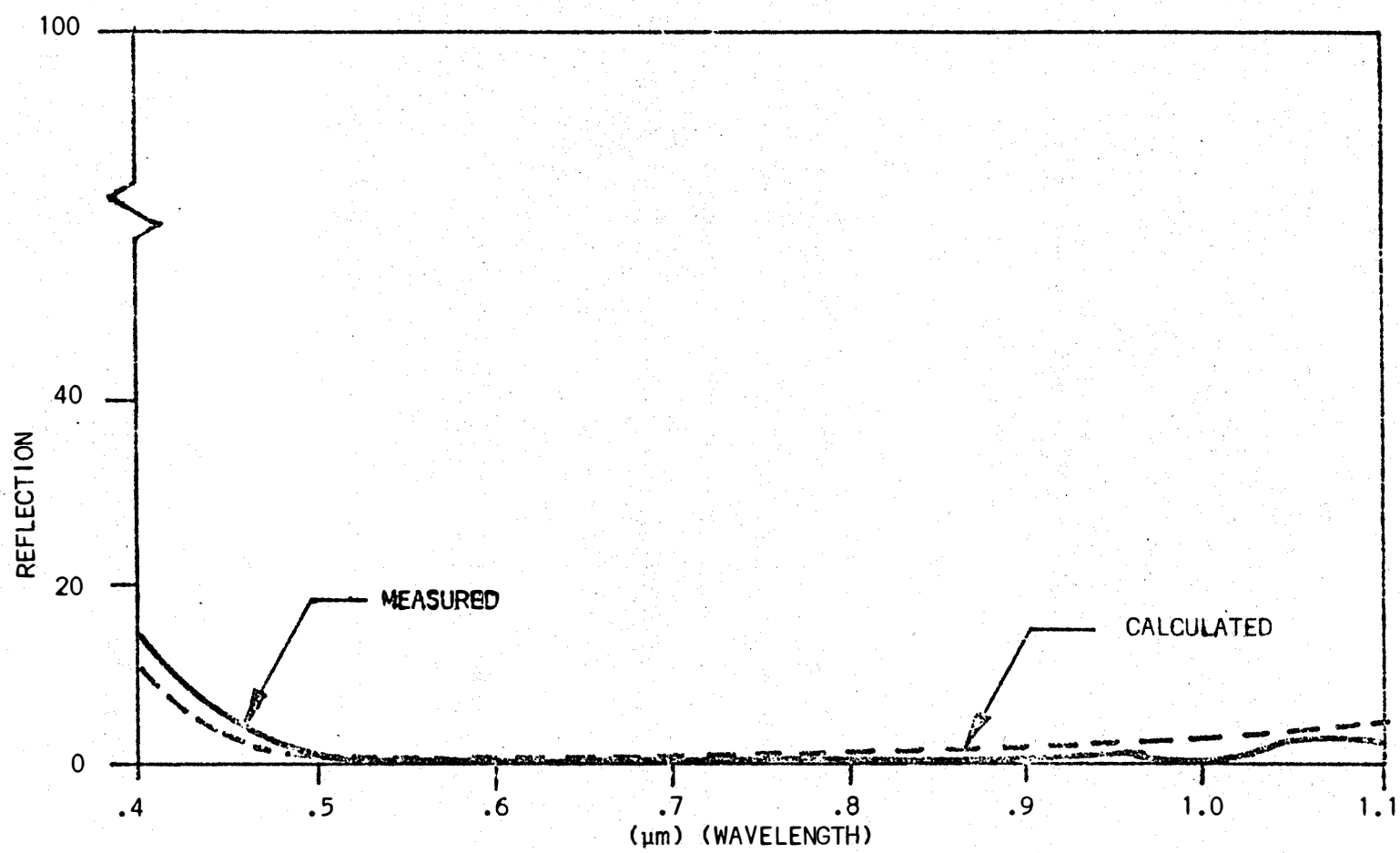

FIGURE 3.5: VARIATION OF REFLECTION COEFFICIENT OF AN AR COATED TEXTURED SILICON CELL AS FUNCTION OF WAVELENGTH.

_____ MEASURED _____ CALCULATED

r_1, r_2 and r_3 are Fresnel reflection coefficients for the interfaces n_0/n_1, n_1/n_2 and n_2/n_3 respectively. These coefficients are given by

$$r_p^{\perp} = \frac{n_{pi} \cdot \cos\theta_{p-1} - n_p \cos\theta_p}{n_{p-1} \cos\theta_{p-1} + n_p \cos\theta_p} \tag{7}$$

$$r_p^{\parallel} = \frac{n_{p-1} \cos\theta_p - n_p \cos\theta_{p-1}}{n_{p-1} \cos\theta_p + n_p \cos\theta_{p-1}} \tag{8}$$

where $p = 1, 2, 3$; θ_p is given by Snells law $n_p.\mathrm{Sin}\theta_p = n_{p-1}\mathrm{Sin}\theta_{p-1}$. Equations similar to R_A apply at wall B. The net reflection coefficient can, again, be calculated by substituting the above expression in equations 1 and 2. Figure 3.5 shows the calculated reflection coefficients for a textured silicon cell with a double layer AR coating consisting of Si_3N_4 (710Å thick) on SiO_2 (100Å). For comparison, figure 3.5 also shows the measured reflectance data of a textured surface with the double layer coating. A good agreement between the theoretical and the experimental curves indicates that ray optics is a good (approximate) technique for analysis of textured surfaces.

3.2 CHOICE OF THIN FILMS

The choice of an appropriate film is based on the following considerations:

(a) The refractive index, n_f, of the film material should be such that

$$n_f \sim \sqrt{n_{silicon}}$$

within the useful range of the spectrum.

(b) Film deposition process should be low cost and compatible with other cell processing steps.

(c) Films should match closely the bulk stochiometry (for negligible absorption).

Although several materials such as Ta_2O_5, Si_3N_4 and SiO have been used, Si_3N_4 appears to be the most promising. Low temperature CVD grown Si_3N_4 films show desirable optical characteristics.

It has been observed that a deposition of a high index layer on the silicon surface leads to a degradation in electrical characteristics of the interface. Use of an intermediate oxide layer is found to alleviate these problems. An SiO_2/Si interface can improve the surface recombination and, hence, improve the cell performance.

3.3 DESIGN OF THE AR COATING

Major object of the design is to determine the parameter values of the coating, required to maximize the external quantum efficiencies of a cell of a known internal quantum efficiency. Although the terms internal and external quantum efficiencies are well known for optical detectors it is instructive to redefine them for a solar cell. The internal quantum efficiency, η_{IQ} is the number of carriers collected by the junction for each photon transmitted into the cell. The external quantum efficiency, η_{EQ}, is defined as the number of carriers collected for each photon incident at the cell surface. Clearly the two quantities are related by

$$\eta_{EQ} = (1-R)\,\eta_{IQ} \tag{9}$$

where R is the reflection coefficient and depends on the bulk material characteristics as well as the characteristics of the surface. R is theoretically determined from expressions given in the previous section for uncoated and coated textured surfaces (also plotted in figures 3.3 and 3.4). η_{IQ} is a parameter that depends on a number of material/device parameters. These include

minority carrier diffusion lengths in the base and the emitter regions, junction depth and the surface characteristics such as recombination velocity and the optical characteristics of the surface*. For a given cell η_{IQ} can be experimentally determined.

Since the parameters R and η_{IQ} depend on the photon energy, equation (9) represents the dependence of the photoresponse of the cell on the photon wavelength for a constant incident flux. To determine the response of the cell to the incident broad-band solar spectrum, whose photon-flux distribution is given by $\Phi(\lambda)$, η_{IQ} must be weighted with respect to $\Phi(\lambda)$.

$$\text{i.e.} \qquad \eta_{IQ}(AM) = \eta_{IQ} \cdot \Phi(\lambda). \tag{10}$$

Notice that for a given input spectrum, equation (10) represents maximum obtainable response (since it represents R = 0 condition in eq. 9). The wavelength dependence of the cell response to the solar spectrum is given by

$$\eta_{EQ}(AM) = [1-R(\lambda)]\, \eta_{IQ}(\lambda) \cdot \Phi(\lambda) \tag{11}$$

and the total integrated response of the cell can be written as

$$\langle \eta_{EQ}(AM) \rangle = \int_{AM} \eta_{EQ}(AM) \cdot d\lambda \tag{12}$$

clearly, the optimum design of an AR coating consists of maximizing the integral on the right hand side of the equation (12).

* Other less dominant factors that contribute to η_{IQ} are dopant profiles and other internal fields.

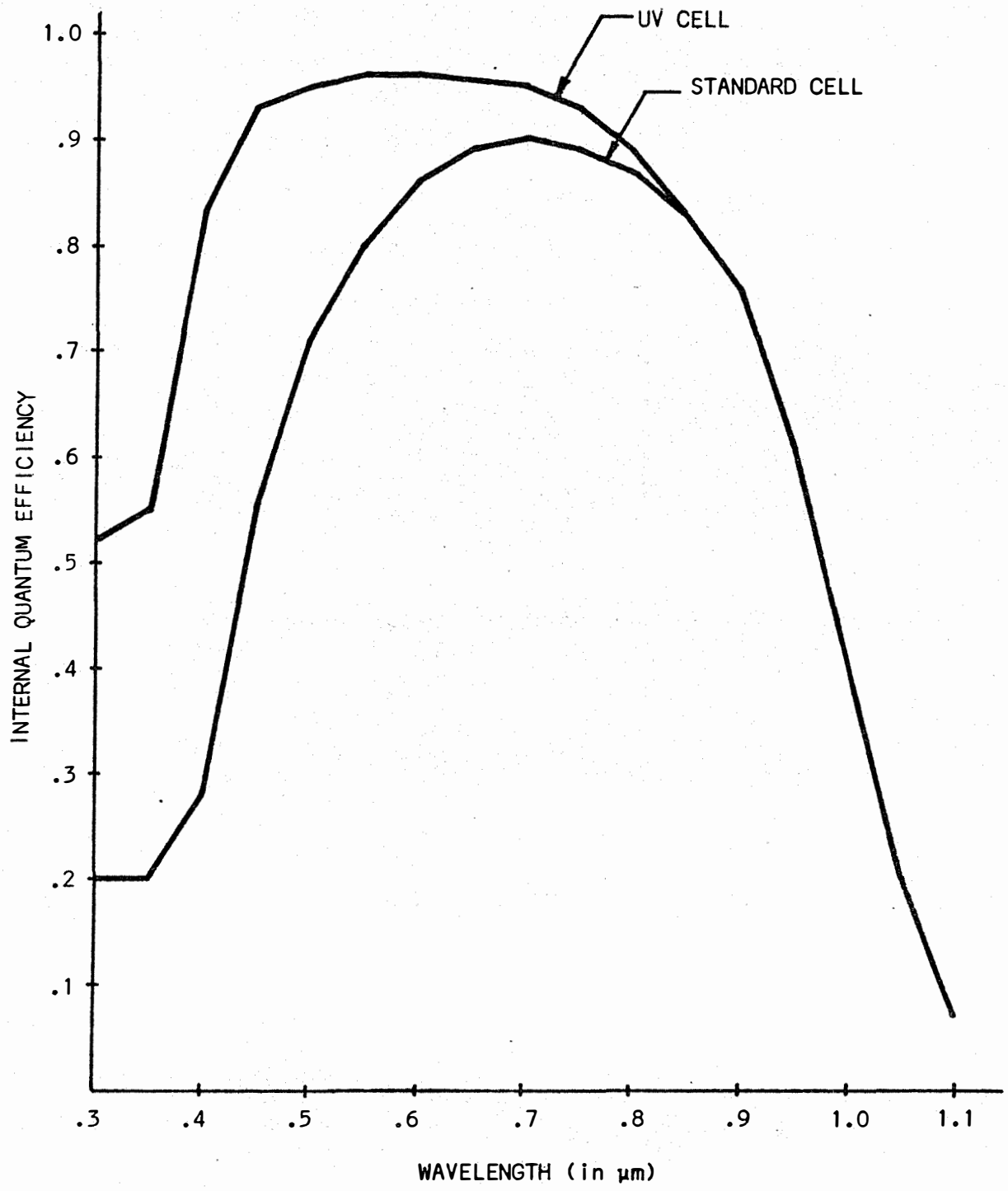

FIGURE 3.6· VARIATION OF INTERNAL QUANTUM EFFICIENCIES OF TEXTURED "UV" AND "STANDARD" CELLS.

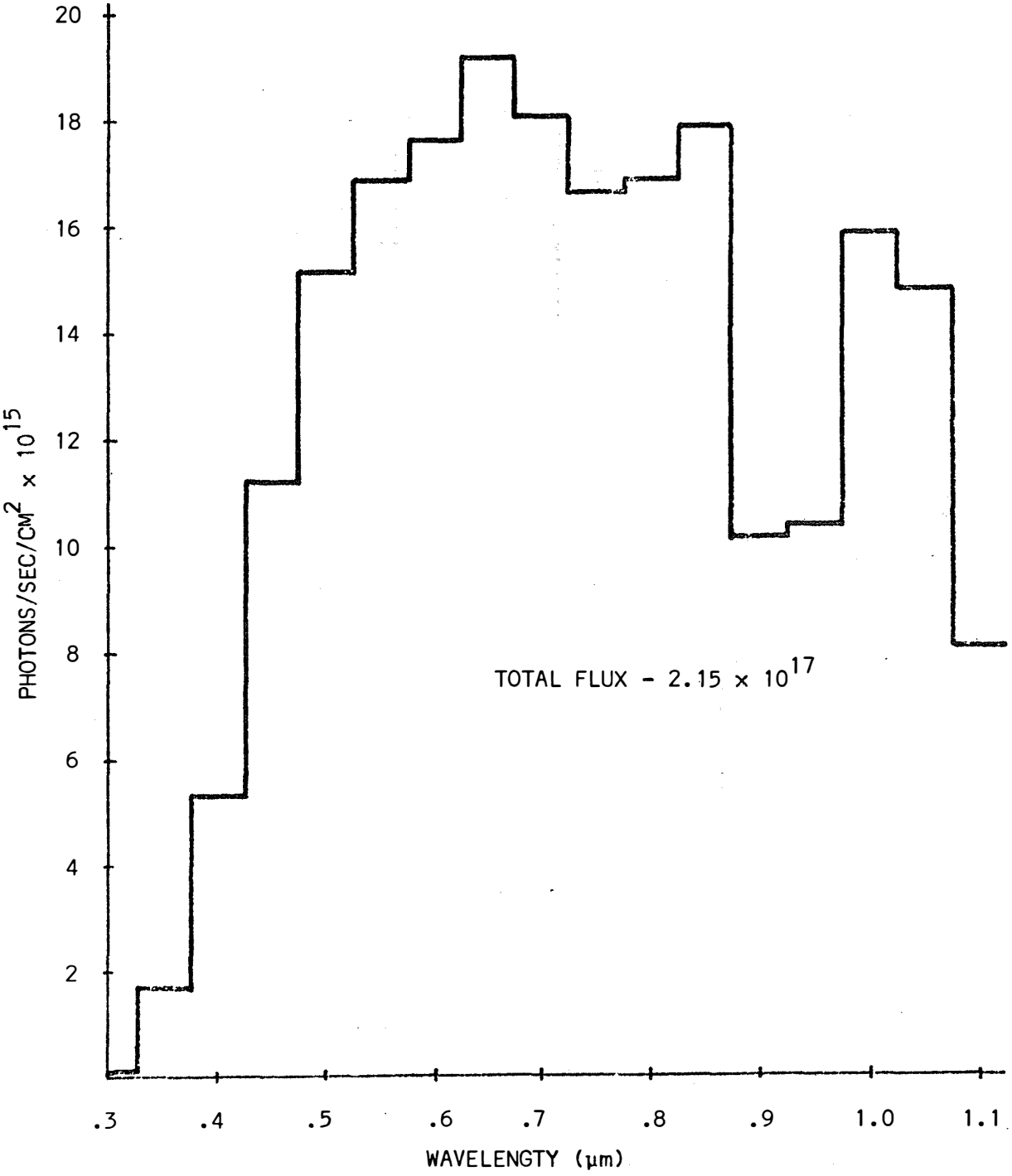

FIGURE 3.7: SPECTRAL VARIATION OF PHOTON FLUX IN THE INCIDENT AM2 SPECTRUM.

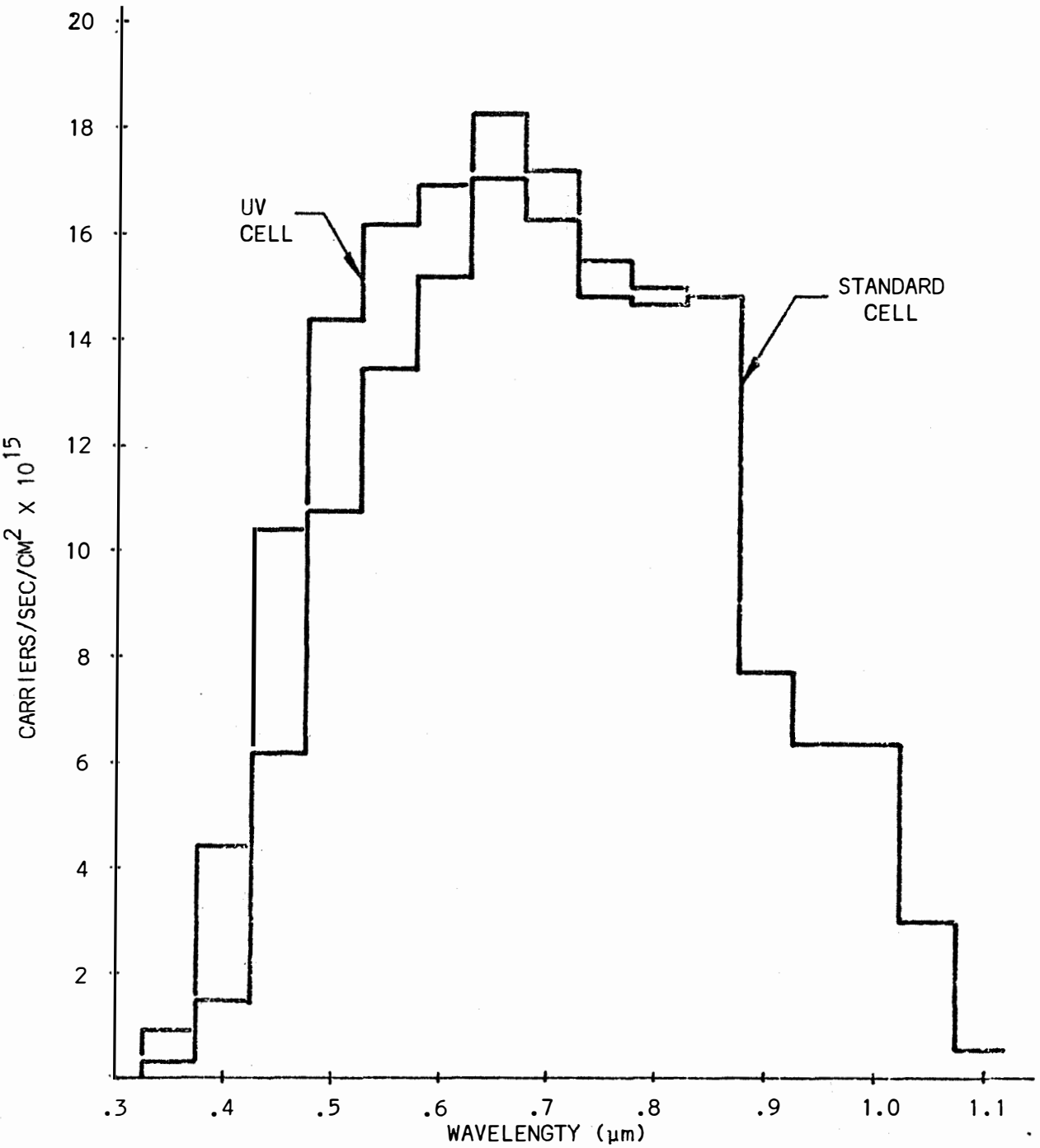

FIGURE 3.8: AM2 PHOTORESPONSE OF TEXTURED "UV" AND "STANDARD" CELLS.

We will elucidate the design by considering examples of two types of cells -- a "standard" cell and a "uv" cell. The internal quantum efficiencies for these cells are assumed to be known and the results of the calculations at various steps of the design will be presented.

Figure 3.6 shows the η_{IQ} of the two cells, in terms of the number of carriers collected per incident Photon, as a function of the photon wavelength. The data selected for this figure corresponds to an average cell of each kind, fabricated typically on Czochralski substrates. Major difference in the responses of the two cells is due to the differences in their junction depths. Junction depth is typically 0.5μm for a "standard" cell and 0.25μm for a "uv" cell; the smaller junction depth of the uv cell results in its higher short wavelength response. The internal photoresponse of the cells to the input solar spectrum can be determined by using equation 10. In these examples we will use AM2 as the incident spectrum. Figure 3.7 shows the photon flux, $\Phi(\lambda)$, due to the AM2 spectrum. The spectrum is shown in the discrete steps of $\Delta\lambda = 0.05\mu m$, and is used in this form in the numerical calculations presented hence forth. This discrete approximation is done to reduce the effort in numerical calculation and yet maintain a good accuracy of the results. The total photon flux with the specturm $0.3\mu m \leq \lambda \leq 1.1\mu m$, is 2.154×10^{17} photons $sec^{-1}cm^{-2}$. Figure 3.8 shows the wavelength dependence of the resultant response i.e. $\eta_{IQ}(AM2)$ for the two cells. The integrated fluxes collected by each cell for AM2 illumination were determined to be 1.47×10^{17} $cm^{-2}sec^{-1}$ and 1.40×10^{17} $cm^{-2}sec^{-1}$ for the "uv" and the "standard" cell respectively. Data in figure 3.8 can now be used in equation 11 and integrated according to the equation 12 to get the total number of carriers collected by each cell due to AM2 illumination. In this example we will use a two-layer AR coating consisting of Si_3N_4 (for the reasons discussed earlier) on 100Å of SiO_2. The optimum thickness of the Si_3N_4 film will be determined from a plot of $\langle\eta_{EQ}\rangle$ vs t_1, where t_1 is the thickness of the nitride film. Figure 3.9 shows the calculated variation

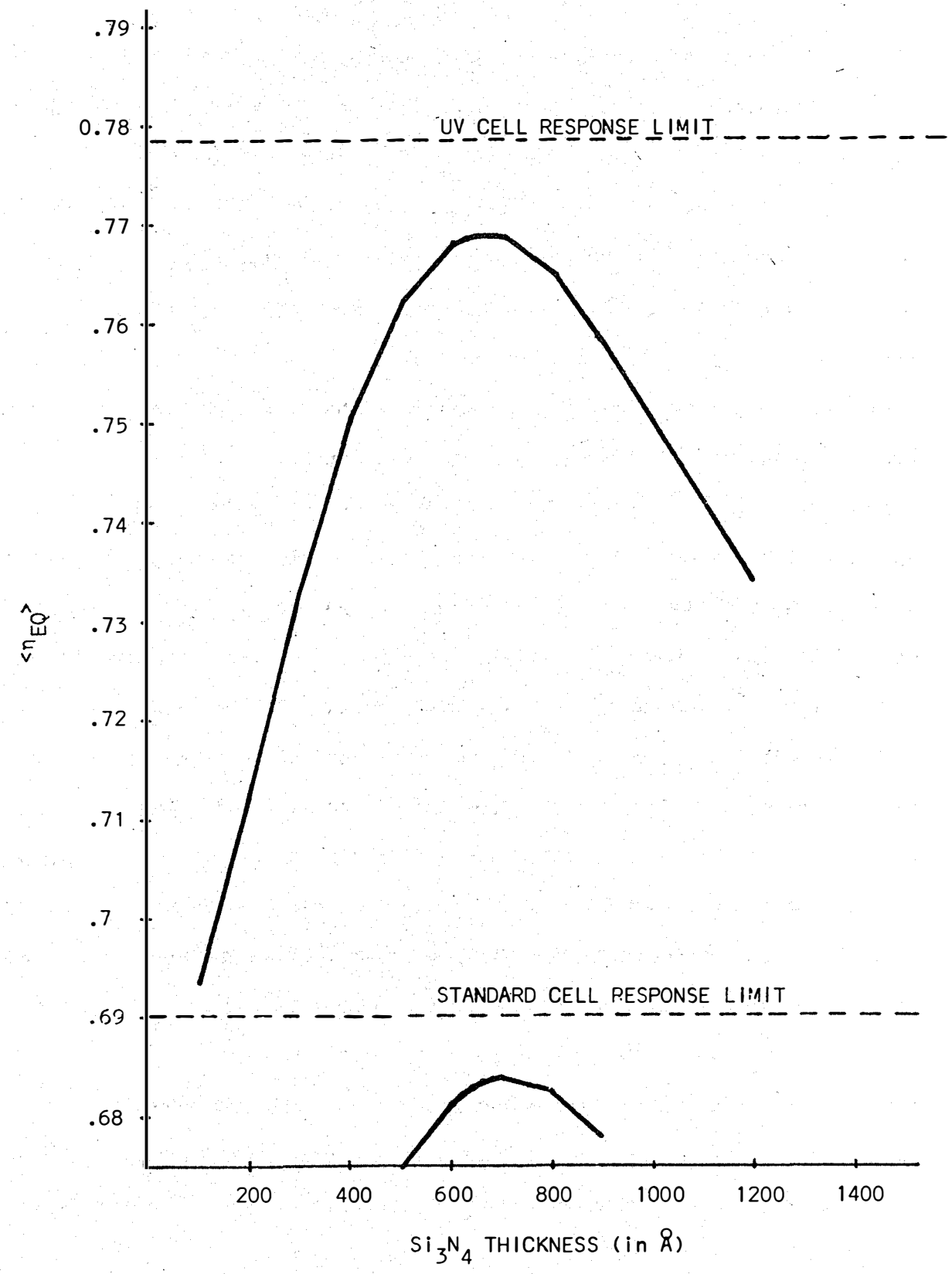

FIGURE 3.9: CALCULATED DEPENDENCE OF $\langle \eta_{EQ} \rangle$ ON THE THICKNESS OF Si_3N_4 FILM (BASED FILM: 100Å SiO_2). THE PLOT IS NORMALIZED WITH RESPECT TO THE TOTAL INCIDENT PHOTON FLUX.

of $\langle \eta_{EQ} \rangle$ as a function of thickness. In calculating $\langle \eta_{EQ} \rangle$ we have used equations 5-8 with the following parameter values: $\theta_o = 54.8^o$, $n_1 = 1.95$, $n_2 = 1.45$, $t_2 = = 100\text{Å}$ and the complex values of n_3 as reported in reference 4. The dotted lines in figure 3.9 represent the maximum attainable efficiency, i.e. for R = 0, in each case. The optimum values of t_1 are found to be 630Å and 650Å for the "uv" and "standard" cells respectively. For the optimum thickness values the total photon flux collected by the "uv" and "standard" cells are 1.661×10^{17} and 1.467×10^{17} $sec^{-1}cm^{-2}$ respectively.

It is useful to compare the optimum thickness values of the AR coating for a textured cell with that of an untextured (Planar) cell. Although in a practical situation the η_{IQ} for textured and untextured cells will be different due to the differences in the refraction characteristics, we will assume η_{IQ} to be the same for two case (for the sake of a fair comparison). Figure 3.10 shows the normalized plots of carrier collection efficiency vs nitride thickness for untextured "standard" and "uv" cells. The maximum collection efficiency occurs at $t_1 = 735\text{Å}$ for the standard cell and $t_1 = 695\text{Å}$ for the uv cell. At these values of t_1, the total photon fluxes collected standard and the uv cells are 1.399×10^{17} $sec^{-1}cm^{-2}$ and 1.561×10^{17} $sec^{-1}cm^{-2}$ respectively. Two important results can be obtained from a comparison between figures 3.9 and 3.10: (i) the optimum thickness for a textured cell is smaller than for a planar cell of the same kind. (ii) Total collected fluxes by textured standard and uv cells are 1.661×10^{17} and 1.467×10^{17}, as compared to 1.561×10^{17} and 1.399×10^{17} respectively. These correspond to 6.4% and 5.5% increase due to texturing. It should be emphasized that this increase is due to reflection alone since we assumed η_{IQ} to be the same for the textured and untextured cell. In reality the increase due to texturing is higher depending on the substrate characteristics.

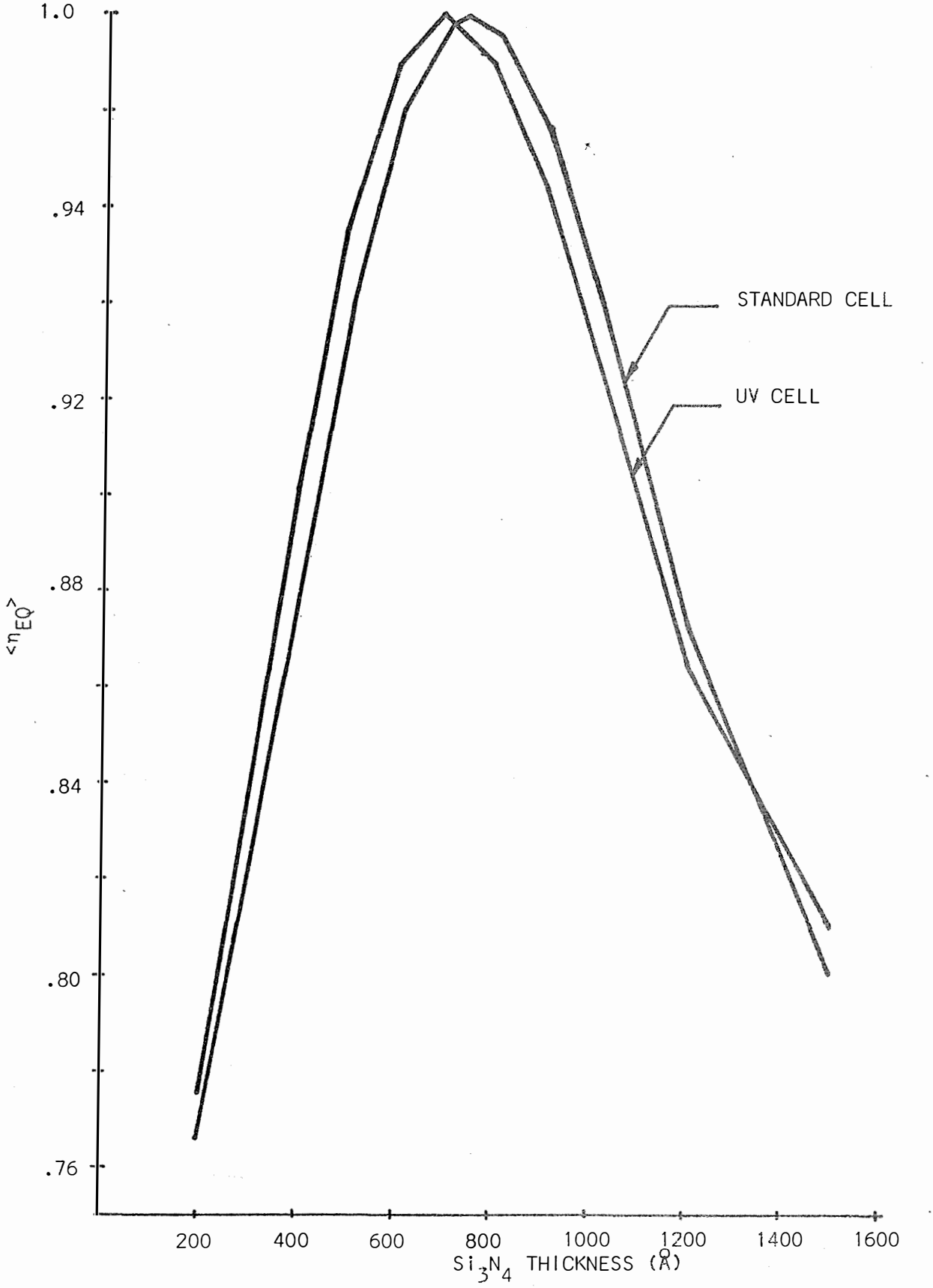

FIGURE 3.10: CURVES SHOWING DEPENDENCE OF $\langle \eta_{EQ} \rangle$ FOR PLANAR "UV" AND "STANDARD" CELLS ON Si_3N_4 THICKNESS.

REFERENCES

1. Dash, W. C., J. Appl. Phys., 27, 1193 91956).
2. C. R. Baraona et al. in Proceedings, Eleventh PHotovoltaic Specialists Conference, IEEE, p. 44.
3. W. L. Bailey et. al., U.S. Patent 4,137,123 (Jan. 1979).
4. Dash, W. C. and Neuman, R., Phys. Rev. 99, 1154 (1955).

APPENDIX

This paper was presented at the 15th IEEE Photovoltaic Specialists Conference held in Orlando, Florida.

OPTICAL CHARACTERISTICS OF TEXTURED (100) ORIENTED SILICON SURFACES -- APPLICATIONS TO SOLAR CELLS

B. L. Sopori and R. A. Pryor

Motorola Inc., Semiconductor Group
Phoenix, Arizona

ABSTRACT

This paper describes theoretical and experimental analyses of optical reflection and refraction characteristics of (100) oriented textured silicon surfaces. Three theoretical approaches (viz "limited ray" optics, diffraction grating, and transmission line) are described which can be selectively used to simplify design analysis to optimize cell performance. Experimental measurements include diffuse reflectance of textured silicon wafers with differently prepared back surfaces, which enable separation of front (textured) surface characteristics from those of the back surface. Measurement of light propagation angles in the air and the substrate are done by direct viewing in visible and IR light. Results of this analysis can be used to design AR coatings and back surface reflectors for optimum cell performance.

INTRODUCTION

Surface texturing for solar cells offers several distinct advantages such as: (i) broadband reduction in surface reflection, which, in conjunction with a thin film coating can lower the net reflection to approximately 3%; (ii) increase in optical absorption within the cell due to increase in optical path; and (iii) a surface preparation technique, in lieu of isotropic etching, to generate a surface potentially low in carrier recombination velocity. Some of these advantages have been indicated previously by other workers; however, there is little quantitative data, theoretical or experimental, which can be used for optimal design of textured cells. Data published to date are concentrated towards study of composite reflectance due to front and back surfaces of a textured wafer. From these data it is not possible to isolate refraction characteristics due to texturing. We have, therefore, carried out theroretical as well as experimental analyses of textured surfaces to determine reflection and refraction characteristics at air/textured silicon (T.S.), air/thin film/T.S. interfaces and their dependences on angle of incidence. This paper describes results of the analysis, particularly emphasizing the basic optical characteristics of textured (100) silicon surfaces which are related to solar cell characteristics. Theoretical approaches are briefly described to indicate the different concepts that can be applied for engineering design to optimize cell performance.

THEORETICAL APPROACHES

Theoretical modelling of textured surfaces is important for understanding and utilizing the characteristics of texturing for improvement in cell performance. However, a rigorous analysis can be unduly complex for most applications regarding solar cells. It is instructive to follow a semi-quantitative approach that can lead to the engineering design of the various parameters necessary for optimization of cell performance. The various important aspects of texturing are: (i) reflection characteristics of an uncoated textured surface (ii) refraction characteristics due to a single textured surface (i.e. semi-infinite substrate) (iii) criteria for the design of a thin film coating to be applied on the textured surface to improve reflection/refraction (iv) interaction of light, diffracted by the front surface, with the back side of the cell and (v) compatibility of the optical design with cell processing; for example, considerations need to be given to the influence of texturing on photolithography, metallization, impurity diffusion profiles, and increased probability of breakage due to exposed cleavage planes.

The theoretical analysis assumes a textured surface to be a two-dimensional pseudo-periodic structure. Several etchants are known which can be controlled to generate regular pyramids or (100) oriented silicon surfaces. These include hydrazine and sodium and potassium based hydroxide solutions. A typical textured surface structure is shown by an SEM photograph in Figure 1. The validity of the pseudo-periodic nature can be clearly demonstrated by observing the diffraction pattern, Figure 2a, due to a well textured surface. The pattern of Figure 2a was generated by shining a HeNe laser beam (λ = .6328Å) normal to the wafer (through a hole in the screen) and photographing the reflected pattern on the screen. This pattern clearly shows four lobes corresponding to a four-fold symmetry. The angular dispersion of the lobes was measured to be 39.2°. Figure 2b is a diffraction pattern due to oblique incidence ($\theta_i = 25^\circ$) of the light on the wafer showing asymmetry of the lobes. If the angle is increased beyond 54.8°, the diffused beam is a single backward travelling lobe i.e. the angle of reflection is negative. It should be pointed out that the regularity of

the pyramids is a condition that yields minimum reflection (as described later). Consequently generation of a clean diffraction pattern can be used to monitor texture etch characteristics.

The foregoing arguments clearly indicate that a textured surface can be analyzed in terms of grating theory. The grating shape may be redrawn for convenience as shown in Figure 3, as a projection on a (100) plane to indicate two orthogonal grating structures along the x and y directions. Due to the large pitch of the grating, several simplifications are evident*, viz

1. Two-dimensional fields due to the grating can be regarded as the superposition of orthogonal fields due to x and y grating components.
2. Ray theory can be applied to determine the aperture field (characteristic of the groove shape).
3. Diffraction of energy (both in reflection as well as transmission) will occur dominantly in one order (±M for each grating component).

We will briefly describe three approaches, commonly used in optics, that are helpful in understanding different characteristics of textured surfaces. Since each approach gives approximate solutions, its range of validity must be confirmed by experiment. These analytical approaches are:

(A) "Limited Ray" Optics. In this analysis one assumes that a ray of light is doubly reflected within the grating grooves for each grating component as shown in Figure 4. This approach is quite simple and gives results which are in close agreement with experiment. Another major advantage of this approach is the ease of extension of the analysis to other cases where one or more thin films may be used for further reduction in reflection coefficients. Magnitude and angular deviations of the optic ray are determined from the Fresnel equations and Snell's law (1). Theoretical results of this analysis are compared with experimental results in the next section.

(B) Diffraction Grating Theory is useful in determining angular dispersion of reflected and refracted beam(s) utilizing grating equations:

$$\sin\theta_i - \sin\theta_p = \frac{p\lambda}{\Lambda} \text{ (for reflection)}$$

$$\sin\theta_i - n\sin\theta_q = \frac{q\lambda}{\Lambda} \text{ (for refraction)}$$

where n is the refractive index and p and q are the diffraction orders. See Figure 5.

(C) Transmission Line (impedance matching) analysis is used to optimize AR coatings for a textured surface. In this approach, the textured surface is replaced by an equivalent planar surface whose impendance is determined from a measured (or calcualted) reflection coefficient. This relation is given by

$$R = \frac{Z_2 - Z_1}{Z_2 + Z_1}$$

where Z_1 and Z_2 represent normalized impedances of the incident medium and textured surface respectively. The AR coating is designed to match Z_1 and Z_2 using a quarter wave plate, Figure 6.

COMPARISON OF THEORY AND EXPERIMENT

In this section we will compare theoretical results with actual measurements. Major emphasis will be on "limited ray" optics theory.

Reflection Characteristics

Figure 4 shows the path of a ray when a textured surface is normally illuminated. From this figure we find that each grating component will lead to two reflected beams emerging at ±39.6° with respect to the incident beam, resulting in a four-fold symmetry of the reflection pattern. The shape of the pattern (i.e. each lobe) corresponds to the aperture field due to the reflecting faces of the pyramids. Clearly we have ignored the edge fields as well as other reflections of the ray between faces I and II (Figure 4) near the bottom of the groove. The effect of these will lead to broadening of the angular dispersion of the lobes. All the same, measured values agree well with theoretical results of this approach. For example measured angular dispersion of the lobes in Figure 2a was 39.2°. Results of calculating the net reflection coefficient considering wavelength dependence of the refractive index of silicon and double reflection are given in Figure 7 (dotted line). Also indicated in this figure is the calculated reflection due to a textured surface with a two-layer coating consisting of 695Å of silicon nitride on 100Å of SiO_2. Actual measurements of the reflection characteristics are shown by solid lines. These measurements were made in a Cary 17 Spectrometer using an integrating sphere. The measured values correspond to single surface reflection*. Clearly a very good agreement exists between theory and the experiment with, expectedly, slightly higher values of calculated reflection.

Transmission Characteristics

A limited ray can also be used for determination of the propagation path within a substrate. Such an analysis will lead to determination of an increased absorption coefficient and hence to

* In conventional texturing peak height range is typically between 10 μm to 15 μm.

* An absorbing back surface was used to eliminate back reflection.

the increase in current density (J_{sc}) of a solar cell as a result of texturing. Figure 8a shows the angular dispersion of transmitted beam into the substrate using Snell's law. Due to the dispersion characteristics of the refractive index of silicon, the angle subtended by the transmitted ray will change with the change in λ. The angles indicated are for λ = 1.15μm (or near the band edge, which is the region where the texturing is mose useful). It should be emphasized that Figure 8a shows that the transmitted ray at the pyramid face is totally internally refracted at face II. This is in contrast to previously used ray approaches where the reflection from face II is ignored (2,3). The present picture matches the observed results described below.

To determine experimentally the angles of the refracted beams, we have used the following "direct viewing" technique. A thick (100) oriented, textured silicon sample is illuminated normally with a HeNe (λ = 1.15 μm) laser beam. Due to the large thickness of the sample (typically 3/8 inch), angular devlations can be determined from separations between diffracted lobes striking the back surface (or emerging from the back surface). Of course, since multiple reflections/refractions can occur between the back and front surfaces, (which can be important in solar cell applications) a careful separation of these effects is necessary. In order to accomplish this, we have carried out experiments with two types of back surfaces: (i) polished and (ii) textured. Figure 8b shows a ray tracing diagram indicating the angles subtended by various reflection orders at the back surface (notice the backward scattering from the front textured surface). Figures 8b and 8c show experimental results of transmission of a λ = 1.15 μm laser beam into a textured substrate with a polished back surface. The refractive angle, measured from Figure 8c for the first reflection, is 29.2°, the same as calculated from the ray approach described in Figure 8a. A non-uniform intensity distribution in the lobes of the same order, Figure 8c, is believed to be due to misalignment of the sample surface with respect to a (100) orientation.

Figure 9 shows similar photographs (taken through an IR viewer) for a sample with both front and back surfaces textured. Figure 9a shows a double exposure photograph (as in 8b); due to background illumination, only one pattern is seen in this figure. Figure 9b is a photograph of the back reflected pattern where the inner bright pattern was partly blocked by placing a black paper directly over it (leading to some light trapping between the paper and the silicon back surface which can be seen emerging along the paper edges). Figure 9c shows a ray tracing diagram corresponding to the doubly textured wafer.

From Figures 8 and 9 (i.e. utilizing ray optics approach) we find that texturing can lead to light trapping effects. Lesser degree of trapping occurs if both surfaces are texured as compared to one side polished. These effects can be observed by carrying out measurements of composite reflectance (including front and back surface) characteristics of thin textured wafers with differently prepared back surfaces. Figure 10 shows these characteristics as a function of wavelength. These measurements were done similar to those shown in Figure 2. The loss in reflectance as a result of back side texture is clearly seen from these figures. Moreover, a comparison of reflectances from wafers with polished and aluminized back surfaces indicates that a polished back does not constitute a complete reflector. Based on these results one can characterize a double sided textured surface with an average power reflectance $\langle R \rangle \approx 0.5$ and single textured surface by $\langle R \rangle \approx 0.6$, in the non-absorbing wavelength range.

Another feature of textured surfaces is the angular dependence of the reflectance, which can be of importance in determining the average influence of texturing with respect to a diurnal change of angle subtended by the sun. Experimentally measured dependence of reflectance on the incident angle is shown in Figure 11 for two cases of illuminating conditions. These correspond to the plane of incidence parallel and 45° with [110] direction. It is seen that a dip in reflectance occurs at ~54° for incidence parallel to [110]; the dip becomes more pronounced for shorter wavelength illumination. These results are compatible with the theory.

APPLICATIONS TO SOLAR CELLS

Texturing can be very useful for improving the performance of solar cells. In this section we will briefly describe various ways in which the optical characterisics of texturing contribute to the improvement in the cell performance, followed by a discussion of some practical difficulties in implementing texturing into solar cell processing. Various factors which contribute to the cell improvement are:

Reduction in Net Reflection

From Figure 3 we see that texturing offers a technique for broad-band reduction in reflection coefficient. For solar cells, the effective reflectance may be defined as

$$\langle R \rangle = \int_{\text{Spectrum}} R(\lambda)\, I_o(\lambda)\, d\lambda \;/\; \int_{\text{Spectrum}} I_o(\lambda)\, d\lambda.$$

where $R(\lambda)$ represents wavelength dependence of the reflectance and $I_o(\lambda)$ is the incident solar spectrum. For a well textured surface, without a thin film coating, the value of $\langle R \rangle \approx 0.1$. A properly designed AR coating will lower the $\langle R \rangle$ value to <0.03. It should be emphasized that optimum design of a thin film AR coating (i.e. determination of the film index and the thickness) for a solar cell involves a convolution of the cell spectral response with the composite surface reflectance $R(\lambda)$ due to texture and the film. Such a procedure is quite involved and will be presented elsewhere (4). However, here we will only present two empirical results which are useful in predicting the changes in the reflectance characteristics of a textured surface due to a thin film deposition. These are: (i) Near-zero reflection conditions are met when film thickness and the index satisfy quarter wave plate conditions for a planar surface,

and, (ii) Deposition of an AR coating leads to a broad minimum (as seen in Figure 7). These results may be expected from the impedence consideration described earlier in the paper.

Increase in Absorption

Due to increase in the angle of light propagation (with respect to the normal to the cell) associated with the texturing, the effective absorption coefficient is increased by a factor $1/\cos\theta$ where θ is the angle of light propagation in the substrate. This effect can play an important role in two cases: (i) Thin cells where this condition essentially leads to an increase in effective thickness, and (ii) When the minority carrier diffusion length of the cell is small.

Light Trapping

It was shown earlier that use of a planar back surface (with or without a metal coating) can give rise to enhanced back reflection thus leading to lighttrapping. This light trapping effect can be used to increase the effective thickness of the substrate.

The use of texturing to improve solar cell performance strongly depends on how compatible the textured surface is with cell processing (also taking into consideration the economic aspects). The factors that influence use of texturing for solar cells are related to the physical and electrical characteristics of the textured surfaces. Various processing steps which are influenced by the physical characteristics are: (i) Photolithography -- line width modulation as well as poor line resolution have been observed to occur as result of exposing photoresist on textured surfaces which possess pyramid heights ~ 15 μm. Clearly this effect can be reduced if the pyramid heights are smaller. Theoretical analysis based on surface impedance considerations leads to the conclusion that pyramid heights can be reduced to 4μm without any observable changes in the reflection/refraction characteristics applicable to solar cells. Experimentally we have observed that well textured surfaces with ~4μm pyramids have shown reflectance characteristics identical to that of ~15μm pyramids. (ii) Metallization -- difficulties can occur in obtaining a uniform coverage of metal on a textured surface. However, no problems have been observed in electrolytic or electroless plating techniques. (iii) Increased probability of breakage due to grooving into (110) cleavage planes i.e. pyramid base edges. Our experience has shown that this problem can be circumvented by proper handling procedures and utilizing processes such as non-contact masking and projection imaging for photoresist exposure.

Electrical characteristics of textured surface junctions may show degradation as compared to the planar junctions, due to: (i) increased surface area; (ii) stresses introduced by metallization; (iii) electrical shunting of the junction by metallized peaks which were broken after junction formation but before metallization and exposed the underlying substrate. Electrical junction characteristics can additionally be influenced by variations which occur in the impurity diffusion profiles over the pyramids.

CONCLUSION

Based on three different approaches, analyses of the optical characteristics of (100) oriented textured silicon surfaces have been presented. It is shown that a well textured surface acts much like a two-dimensional diffraction grating. Measured reflection characteristics agree well with ray theoretical calculations. Direct viewing of light propagation paths (visible light for reflection and IR for transmission) has been used to determine the angular dispersion of the diffracted beams. Various modes of utilizing texturing for the improvement in solar cell characteristics have been described. It is shown that the major advantage of texturing can be due to increased absorption if (i) the minority carrier diffusion length of the cell is small (ii) the cells are thin.

We have also shown that pyramid heights need to be only ~4μm to be effective in obtaining desired characteristics. This property can lead to considerable simplification in cell processing.

REFERENCES

1. M. Born and E. Wolf "Principles of Optics" Pergamon Press, 1970.
2. R. A. Arndt, J. F. Allison, J. G. Haynes and A Meulenberg, in the Proceedings of 11th IEEE Photovoltaic Specialists Conference, 1975, (and references there).
3. M. G. Coleman, R. A. Pryor, L. A. Grenon and I. A. Lesk, Annual Report, 1977, JPL Contract #954363.
4. B. L. Sopori and R. A. Pryor, "Design of AR Coatings for Textured Solar Cells", to be published.

ACKNOWLEDGMENT

The authors would like to thank Edward Pastirik and Kelly Nicely for texturing the samples, Marge McClure and Tom Nilsson for carrying out some measurements and I. A. Lesk for many valuable discussions regarding this work.

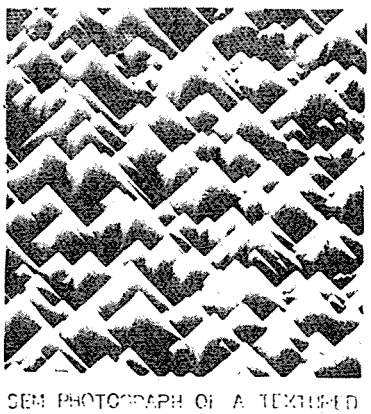

FIGURE 1. SEM PHOTOGRAPH OF A TEXTURED (100) ORIENTED SILICON SURFACE (TEXTURE #4).

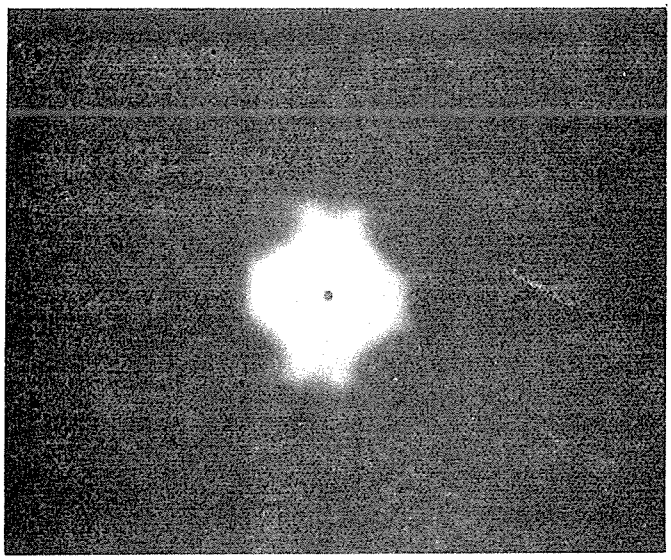

A

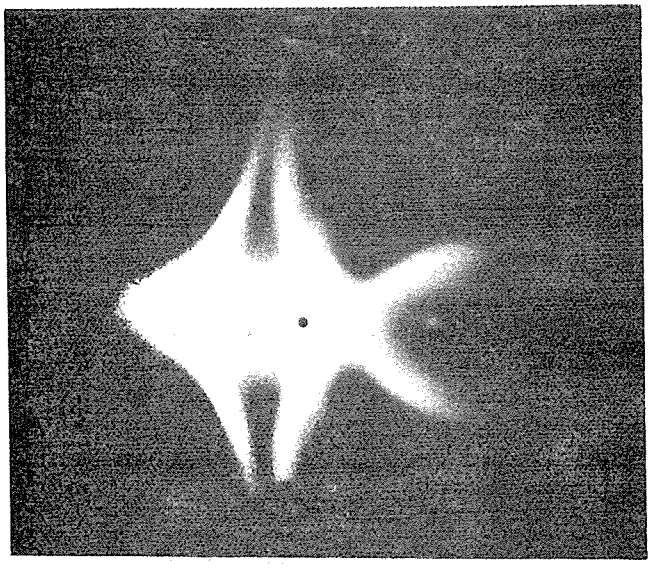

B

FIGURE 2. REFLECTED BEAMS CORRESPONDING TO INCIDENCE OF A HeNe LASER BEAM (A) NORMAL INCIDENCE (B) OBLIQUE INCIDENCE.

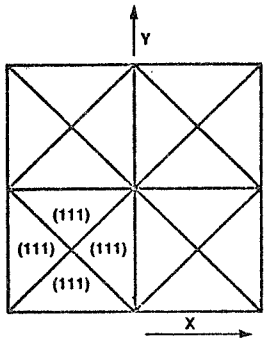

FIGURE 3. ILLUSTRATIONS SHOWING PERIODIC STRUCTURE OF A TEXTURED SURFACE, PROJECTION ON (-100) PLANE.

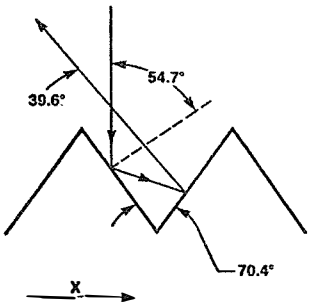

FIGURE 4. ILLUSTRATION OF RAY PROPAGATION FOR X-GRATING COMPONENT.

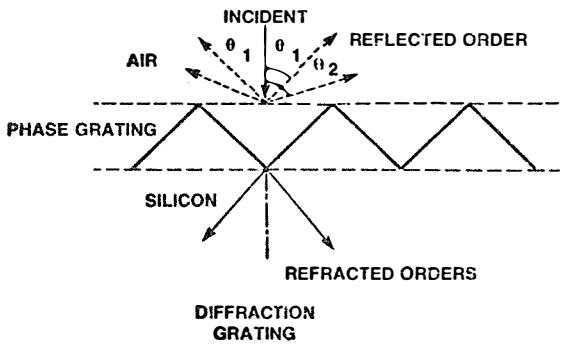

FIGURE 5. ILLUSTRATION OF DIFFRACTION GRATING APPROACH.

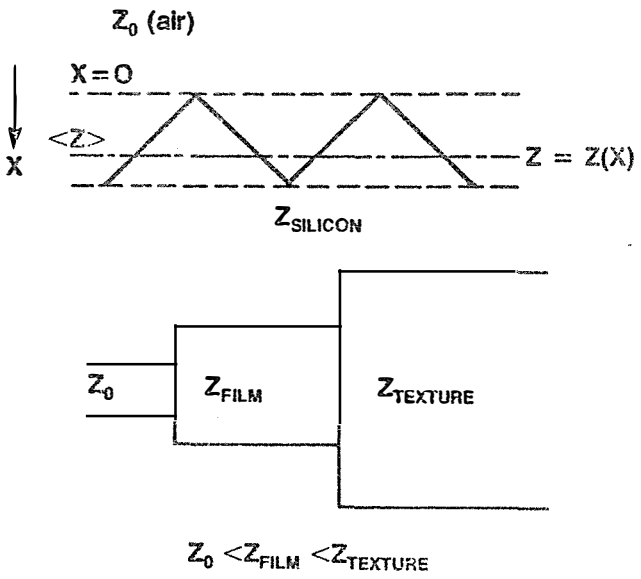

FIGURE 6. ILLUSTRATION OF TRANSMISSION LINE APPROACH.

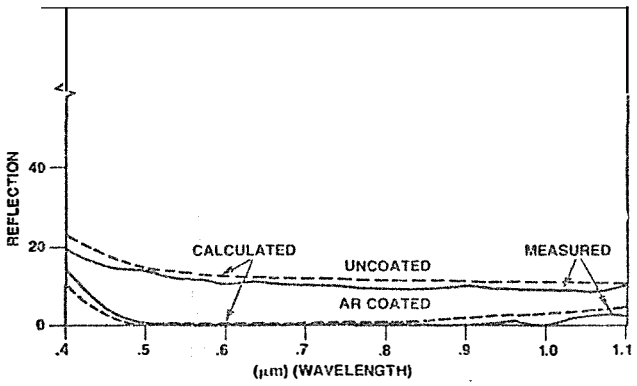

FIGURE 7. COMPARISON OF EXPERIMENTAL AND THEORETICAL REFLECTION CHARACTERISTICS FOR TEXTURED AND TEXTURED + AR COATED SURFACES. AR COATING WAS DESIGNED FOR MINIMUM WEIGHTED REFLECTION FOR AM1.

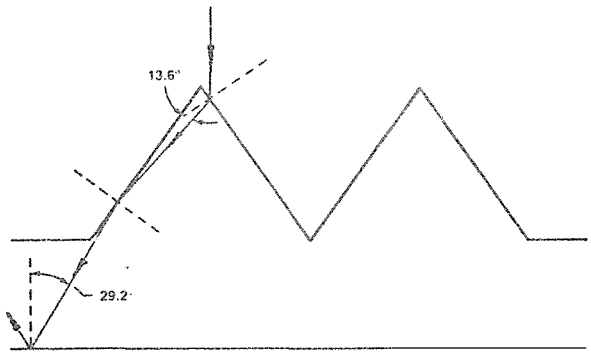

A

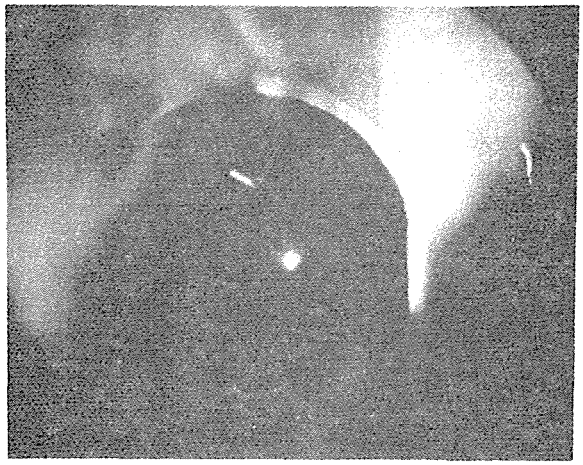

B

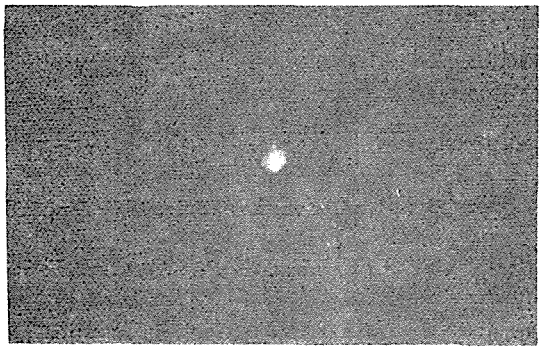

C

FIGURE 8. (A) RAY TRACING FOR FRONT TEXTURED (BACK POLISHED) WAFER.
(B) A DOUBLE EXPOSURE OF WHITE LIGHT ILLUMINATED (POLISHED) BACK SURFACE AND A TRANSMISSION PATTERN DUE TO 1.15 μm LASER BEAM.
(C) TRANSMISSION PATTERN SHOWING VARIOUS BACK SURFACE REFLECTION ORDERS.

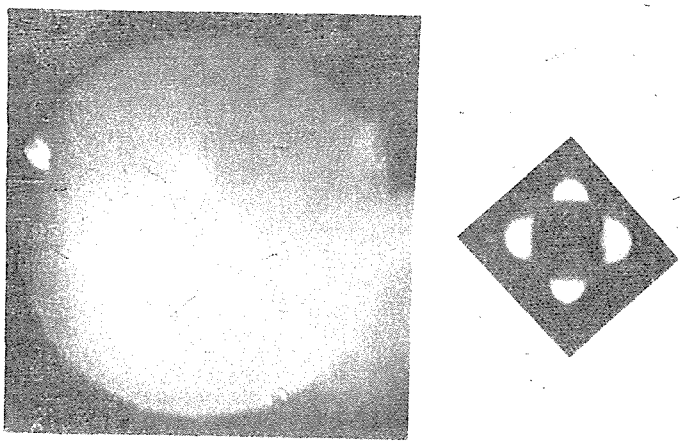

A

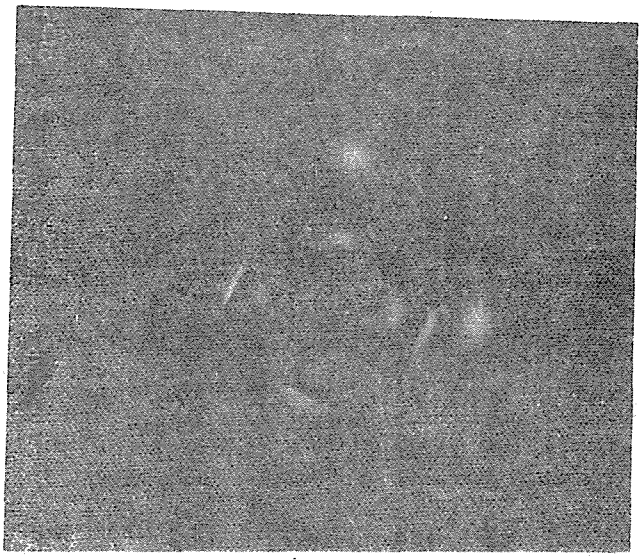

B

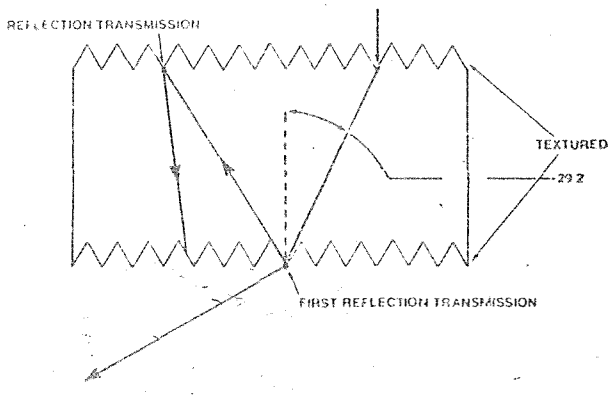

C

FIGURE 9. PATTERN VIEWED IN A DOUBLE SIDED TEXTURED WAFER.

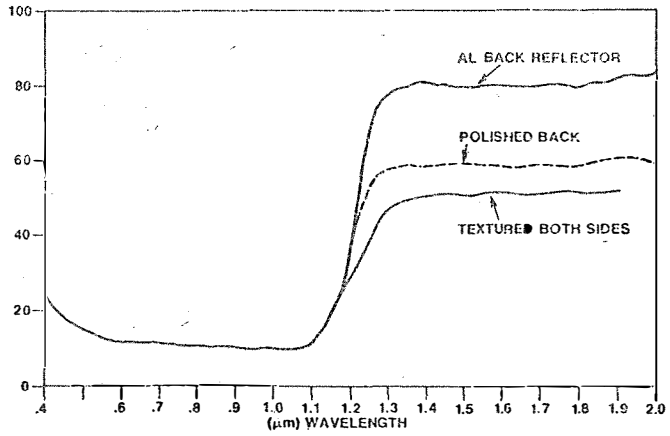

FIGURE 10: EXPERIMENTAL REFLECTION CHARACTERISTICS OF A TEXTURED (FRONT) SURFACE FOR DIFFERENTLY PREPARED BACK SURFACE.

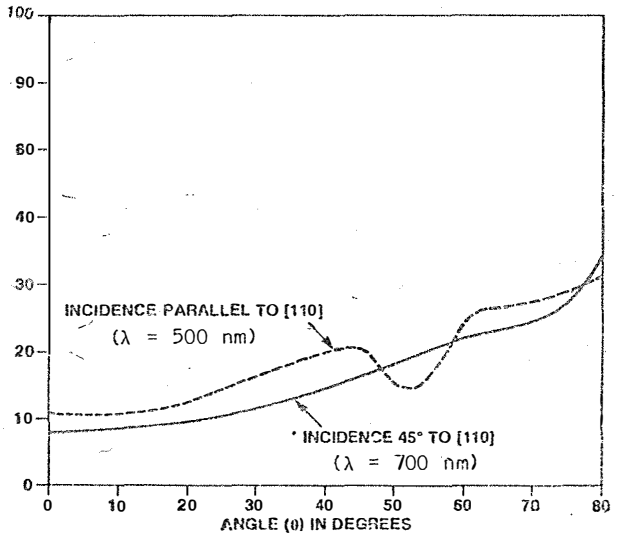

FIGURE 11. ANGULAR DEPENDENCES OF REFLECTANCE FOR TWO DIFFERENT ORIENTATIONS OF TEXTURED SURFACE. (A) PLANE OF INCIDENCE ALONG [110] DIRECTION (B) PLANE OF INCIDENCE 45° WITH [110] I.E. ALONG PYRAMID EDGES.

☆U.S. GOVERNMENT PRINTING OFFICE: 1981-740-145/2461